A LARGE LATE-GLACIAL ERUPTION OF THE HUDSON VOLCANO, SOUTHERN CHILE

by

DEREK JAMES WELLER

B.A. University of Colorado, 2010

A thesis submitted to the

Faculty of the Graduate School of the

University of Colorado in partial fulfillment

of the requirement for the degree of

Masters of Science

Department of Geological Sciences

2015

This thesis entitled:

A Large Late-glacial Eruption of the Hudson Volcano, Southern Chile
written by Derek James Weller
has been approved for the Department of Geological Sciences

_____
Dr. Charles Stern

_____
Dr. G. Lang Farmer

Date_____

The final copy of this thesis has been examined by the signatories, and we
Find that both the content and the form meet acceptable presentation standards
Of scholarly work in the above mentioned discipline.

Weller, Derek James (M.S., Geological Sciences)

A Large Late-glacial Eruption of the Hudson Volcano, Southern Chile

Thesis directed by Dr. Charles Stern

ABSTRACT

Lakes formed in the Aysén region of southern Chile after the retreat of mountain glaciers, beginning by at least ~17,900 cal yrs BP, contain numerous late-glacial and Holocene tephra layers derived from >70 eruptions of the volcanoes in the region, including Hudson, the southernmost in the Andean Southern Volcanic Zone (SVZ). Sediment cores from six of these lakes each contain an unusually thick late-glacial age tephra layer, which based on its distribution and bulk trace-element composition was derived from a large explosive eruption of the Hudson volcano between 17,300 and 17,440 cal yrs BP, and is termed Ho. In these cores, located ~100 km northeast of Hudson, the Ho tephra layers range between 35 to 88 cm in thickness. Comparison with three previously documented large explosive Holocene Hudson eruptions (H1, H2, H3 1991 AD) suggests that Ho was larger, with an estimated tephra volume of >20 km^3, the largest post-glacial eruption documented for any volcano in the southern Andes. In total, Hudson has erupted ≥45 km^3 of pyroclastic material in the last ~17,500 years, making it the most active volcano in the southern Andes in terms of the total volume of pyroclastic material erupted since the beginning of deglaciation in the region. Chemical stratification is not seen in the Ho deposits, but this eruption was bi-modal, with a much greater proportion of dark glassy basaltic-andesite dense fragments and pumice, which range between 55 to 59 wt % SiO_2, and volumetrically less significant lighter colored dacite pumice with 66 wt % SiO_2. In contrast, H1 was andesitic in composition, H2 was more felsic than H1, being composed essentially of

dacite, and although H3 in 1991 AD was again bi-modal, it erupted a much smaller proportion of mafic compared to felsic material than Ho. Thus, the repetitive large explosive eruptions of Hudson volcano have evolved to progressively less mafic overall compositions from late-glacial to historic times, and their volumes have decreased. All analyzed phases of different Hudson eruptions, have similar Sr-isotopic composition (0.70444 ± 0.00007), indicating that crystal-liquid fractionation rather than crustal assimilation was the main process responsible for these chemical variations.

ACKNOWLEDGMENTS

I would like to thank my mother, father and three brothers for their continued support. I wouldn't have been able to do this without you. I also would like to thank the Granato and Harris families for always being there for me and my family. Additionally, I would like to thank my advisor Chuck and my committee members for their comments that improved the quality of this thesis. Finally, I would like to thank Carmen Miranda, Patricio Moreno, Rodrigo Villa-Martinez, M. Kaplan, M. Fletcher, I. Vilanova, W. Henriquez and E. Simi for obtaining the cores and assistance in the lab selecting the samples.

CONTENTS

FIGURES

TABLES

CHAPTER I

INTRODUCTION

A prevalent geologic feature along the western coast of South America is subduction related volcanism. Andean volcanism results from the subduction of Nazca and Antarctic Plates below the continental lithosphere of western South America (Fig 1 inset). There are over 200 Pleistocene and Holocene arc volcanoes along the continental margin of South America. These volcanoes are grouped into four distinct segments called the Northern (NVZ; 2^{o}N-5^{o}S), Central (CVZ: 14^{o}S-28^{o}S), Southern (SVZ; 33^{o}S-46^{o}S) and Austral (AVZ; 49^{o}S-55^{o}S) volcanic zones.

In Chile alone, the Andean Southern Volcanic Zone consists of >70 Pleistocene and Holocene composite stratovolcanoes and large volcanic fields. In the northern portion of the SVZ (33.3^{o}S-34^{o}S) the volcanoes are a narrow chain situated along the Chile-Argentina boarder but between 34.4^{o}S-39.5^{o}S the arc widens and volcanic centers occur in both Chile and Argentina. South of 39^{o}S the SVZ once again consists of a narrow chain of volcanoes and south of 42^{o}S all of the arc volcanoes are located in Chile. The southernmost portion of the Andean Southern Volcanic Zone (Fig. 1; Stern 2004; Stern et al. 2007; Volker et al. 2011) is composed of several large composite volcanoes, including Melimoyu, Mentolat, Macá, Cay, and Hudson, and also many (>15) small monogenetic minor eruptive centers (MEC) along the Liquiñe-Ofqui Fault System (LOFS) and surrounding the major volcanic centers (D'Orazio et al. 2003; Gutiérrez et al. 2005; Vargas et al. 2013).

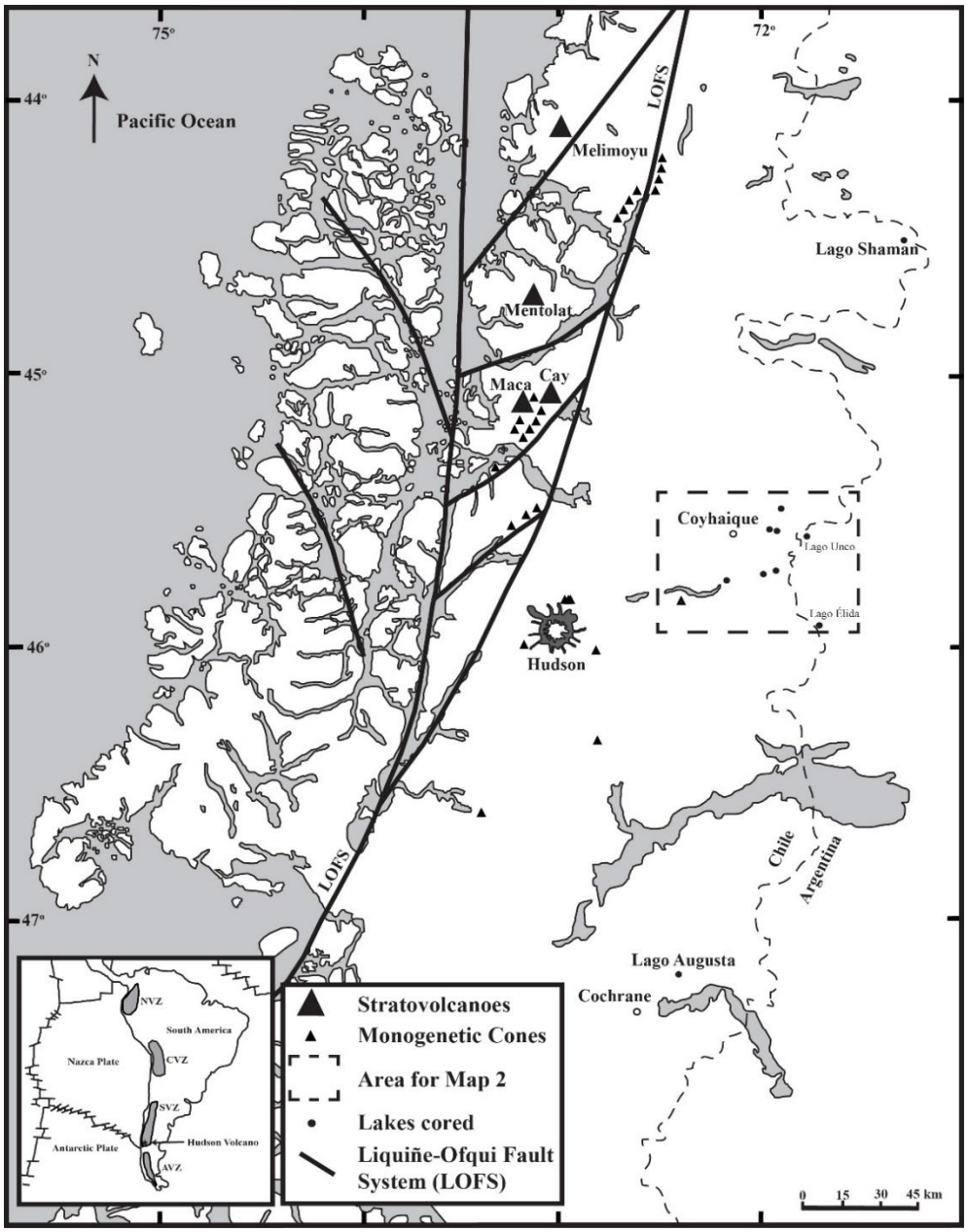

Figure 1. Map of southernmost portion of the SVZ showing the location of Hudson as well as Macá a, Cay, Mentolat and Melimoyu volcanoes. Also shown are the locations of some of the monogenetic centers along the Liquiñe-Ofqui Fault System (LOFS) and surrounding Hudson, Macá and Cay (D'Orazio et al. 2003; Gutiérrez et al. 2005; Vargas et al. 2013). The box shows the area of the map which locates the lakes from which cores were obtained (Fig. 2; Miranda et al. 2013). Lago Shaman (de Porras et al. 2012) occurs further to the northeast and Lago Augusta to the south near Cochrane (Villa-Martínez et al. 2012).

Lacustrine sediment cores from seven lakes formed in this region of Chile (Figs. 1 and 2) after the initiation of the retreat of mountain glaciers, which started by at least ~17,900 cal yrs

BP (Miranda et al. 2013), each contain multiple tephra layers derived from an integrated total of >70 explosive eruptions of these volcanoes (Figs. 3 and 4). These eruptions span the period of climate change at the transition from the glacial to the post-glacial warm period and extend through the Holocene.

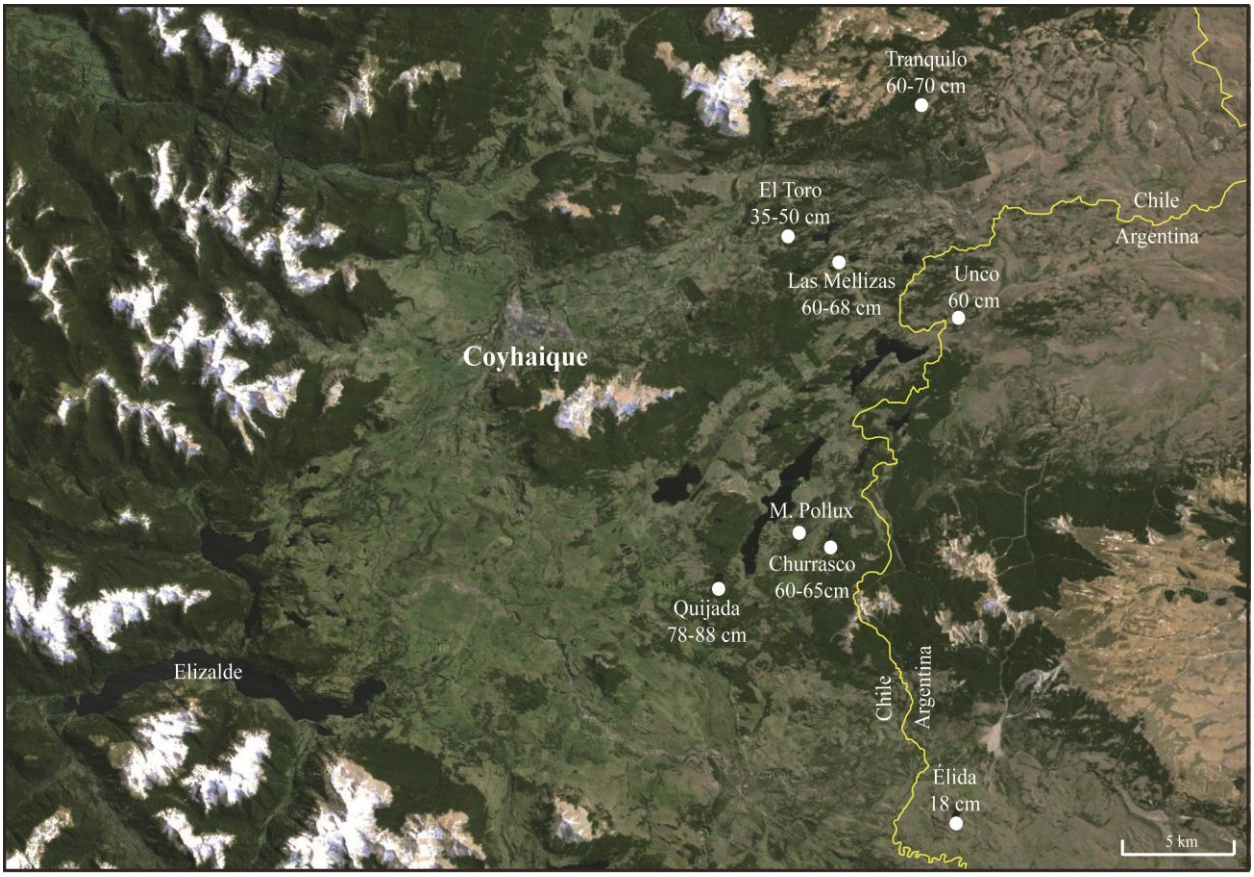

Figure 2. Google Earth Image showing the location of the lakes from which the cores (Figs. 3 and 4) discussed in the text were taken and the thickness range for the Ho deposits within each lake.

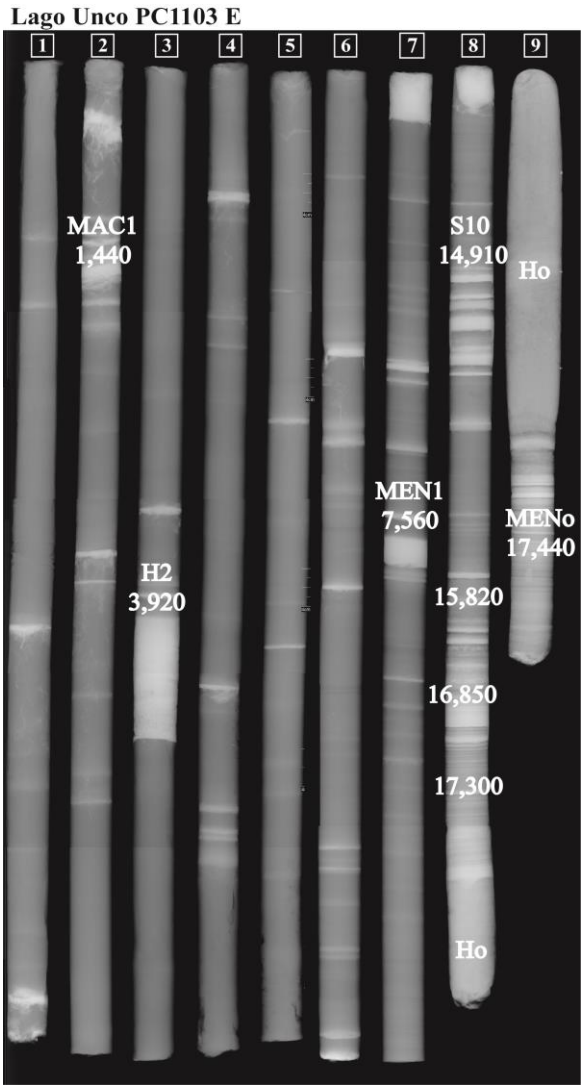

Figure 3. X-ray image of the 8.5 x 1 meter sections of the in total 8.5 meter core from Lago Unco, >100 km east of Hudson volcano (Figs. 1 and 2). The >70 multiple different tephra in this core appear as white layers due to their higher density compared to the predominantly organic lake sediments in which they are preserved. The large late-glacial Ho tephra is 60 cm thick, extending from core section #8 at 78 cm to section #9 at 38 cm. Ho is constrained in age in this core by dates in the organic rich sediments overlying and underlying the Ho tephra as between 17,300 and 17,440 cal yrs BP in age (Table 1 in the Appendix; Miranda et al. 2013).

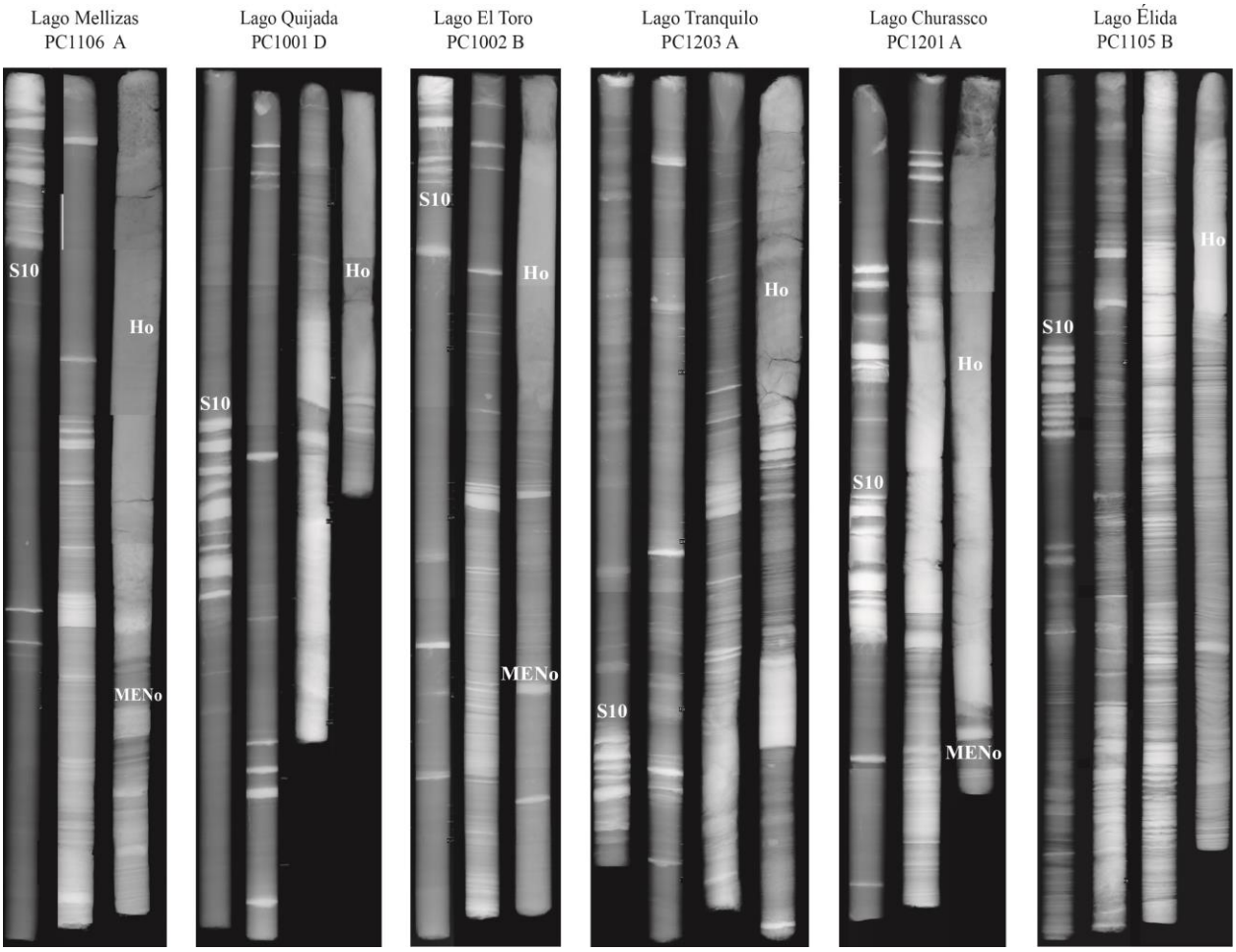

Figure 4. X-ray images for 6 of the other lakes where the Ho tephra has been observed. The large late-glacial Hudson eruption is labeled Ho, with the sequence of 10 (S10) closely spaced eruptions and MENo as reference deposits for each core. Each section of each core is approximately 1 meter in length and 4 cm wide.

Specific source volcanoes for some of the tephra layers in these cores have been identified from their trace-element chemistry. For example, lavas, pumice and tephra derived from Hudson volcano have distinctively elevated concentrations of large-ion-lithophile elements, (LIL), rare-earth-elements (REE), and high-field-strength-elements (HFSE) compared with samples of similar silica content derived from other volcanoes in both the Andean SVZ and Austral Volcanic Zone (AVZ, Fig. 5; Futa and Stern 1988; Stern 1991, 2008; Naranjo and Stern 1999; Gutiérrez et al. 2005). In contrast, tephra derived from eruptions of Mentolat have notably

lower concentrations of LIL, REE and HFSE (López-Escobar et al. 1993; Naranjo and Stern 2004; Stern et al. 2013) while deposits from Macá, Cay and the MEC have intermediate trace element abundances compared to Mentolat and Hudson. Based on these chemical characteristics, and their stratigraphic depth in the cores, some of the previously identified and dated large explosive eruptions of Hudson, such as H2 at ~3,920 cal yrs BP (Naranjo and Stern 1999), of Mentolat, such as MEN1 at 7,560 cal yrs BP, and MAC1 at 1,440 cal yrs BP (Naranjo and Stern 2004; Stern et al. 2013), have been recognized in these cores (Fig. 3).

Hudson (45°54'S; 72°58'W), which is the southernmost volcanic center in the SVZ, has had three large explosive eruptions during the Holocene (Stern 1991, 2008; Scasso et al. 1994; Naranjo and Stern 1998; Kratzmann et al. 2009). Sixteen sediment cores from the seven lakes each contain an unusually thick late-glacial age tephra layer (Tables 1 and 2 in the appendix; Figs. 3 and 4) resulting from a very large eruption, which based on both its bulk trace-element composition (Fig. 5) and distribution (Fig. 6), was derived from Hudson volcano and is termed Ho (Weller et al. 2013).

In this thesis I characterize some of the physical and chemical features of the late-glacial Ho eruptive products and make an assessment of the total eruptive volume of this and other explosive eruptions of the Hudson volcanic center since the beginning of deglaciation in southern Chile.

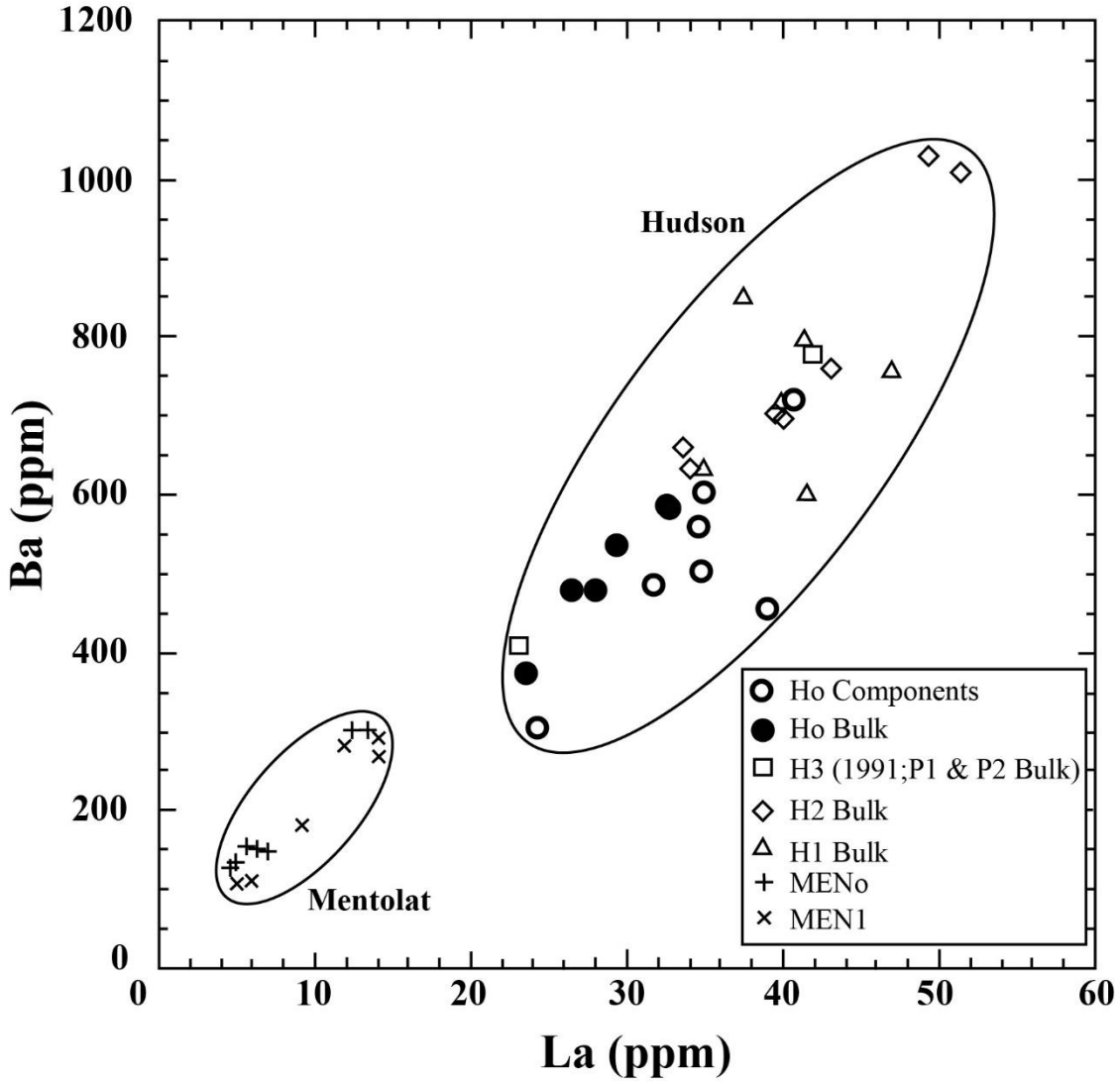

Figure 5. La vs. Ba plot showing the fields occupied by the different eruptive products from Hudson (H3 in 1991 AD, H2, H1 and Ho) and Mentolat Volcano. Hudson eruptive products are elevated in LIL, HFSE and REE compared to Mentolat and other southern SVZ tephras.

Geologic/Tectonic Setting

The Hudson Volcano is the southernmost volcano in the Andean Southern Volcanic Zone (SVZ; 33-46°S; Stern 2004; Stern et al. 2007). Volcanism in this section of the Andean cordillera is the result of subduction of the Nazca Plate under the South American continent (Fig. 1). Further to the south is the Austral Volcanic Zone (AVZ; Stern and Kilian 1996), in which volcanism is the result of the subduction of the Antarctic Plate underneath the southern portion

of the South American Plate. In between the AVZ and Hudson is a ~350 km gap in the active volcanic arc that lies just south of where the Chile Rise, an active spreading center that separates the Antarctic and Nazca Plates, has been subducted under the South American Plate (Cande and Leslie, 1986). Marine geophysical data indicate that the Chile Rise first collided with the Chile Trench near Tierra del Fuego, and has migrated north along the continental margin over the last 15-20 Ma to its current location (Cande and Leslie 1986; Nelson et al. 1994).

Cembrano and Herve (1996) suggest that there is a strong connection between the arc-parallel Liquiñe-Ofqui Fault System (LOFS; Fig. 1) and the location of the volcanic centers of the SVZ. The LOFS results from a combination of oblique subduction of the Nazca Plate and the impingement of the Chile Rise against the continent. Most of the southern SVZ volcanoes are located along or to the west of the LOFS. Hudson volcano, in contrast, is situated approximately 30 km east of this fault zone (Naranjo and Stern 1998). Numerous monogenetic minor eruptive centers (MEC) are also roughly aligned along the LOFS trend (Fig. 1; Gutiérrez et al. 2005), and others surround the Hudson, Macá and Cay edifices as well.

The Quaternary volcanoes of the southern SVZ are located on a portion of the Northern Patagonian Batholith composed of mainly tonalites and granodiorites (Pankhurst et al. 1999; D'Orazio et al. 2003; Gutiérrez et al. 2005). This Cretaceous to late Miocene intrusive complex, which is ~1000 km in length and extends across the length of the southern SVZ (41°S-52°S) formed by episodic magmatic events over a 125 Ma time interval (Pankhurst et al. 1999).

The calc-alkaline magmatism produce by the southern SVS volcanoes are generally high Al_2O_3 basalts and basaltic andesites (Futa and Stern 1988; López-Escobar et al. 1993; D'Orazio et al. 2003), with only minor andesites, dacites and rhyolites. Hudson generates magmas which are compositionally distinct from the other southern SVZ volcanic centers such as Mentolat (Fig.

5), Macá and Cay (Fig. 8). Analyzed samples from Hudson range from basalts to dacites with high TiO_2, FeO, Na_2O, and K_2O relative to rocks of similar silica content erupted from other volcanic centers in the southern SVZ (Futa and Stern 1988; Stern 1991, 2008; López-Escobar et al. 1993; Naranjo and Stern 1998; D'Orazio et al. 2003; Gutiérrez et al. 2005; Kratzmann et al. 2009). Hudson's extrusive rocks are also rich in incompatible trace elements, which include LIL, REE, and HFSE, compared to samples from other southern SVZ and AVZ volcanoes with similar silica content (Stern 1991, 2008; Naranjo and Stern 1998).

Hudson Eruptions

The Hudson caldera was first identified as a volcano only after a small Plinian eruption and lahar in 1971 (Tobar l972; Fuenzalida and Espinosa 1974; Fuenzalida l976; Cevo l978; Best l989, l992). Hudson erupted as recently as October 2011 and K-Ar dates indicate that this volcano has been active for at least the last 1 Ma (Orihashi et al. 2004). The most recent large explosive eruption from Hudson (H3 in 1991 AD) occurred on August 8, 1991. It began with an initial phreatomagmatic event (Phase 1) which erupted through a 400 m crater and a 4 km long fissure in the northwestern portion of the caldera (Naranjo et al. 1993; Scasso et al. 1994; Kratzmann et al. 2009; Wilson et al. 2011, 2012). The paroxysmal phase (Phase 2) began on the 12th of August with a Plinian style eruption from an 800 m wide crater located in the southwestern portion of the caldera. This phase of the eruption continued on and off for three days before ceasing on the 15th of August. The tephra fallout from Phase 2 was dispersed in a ESE direction covering a narrow, elongated sector of southern Patagonia (Scasso et al. 1994; Wilson et al. 2011, 2012). This eruption produced at least 4 km^3 of volcanic material, but the overall volume is likely to have been larger because tephra was also deposited into the sea.

Tephra from this eruption ranges in composition from basalt during Phase 1 to trachyandesite and dacite during Phase 2, with a distinct gap between 54 to 60 wt % SiO_2 separating the two phases (Kratzmann et al. 2009). Furthermore, Kratzmann et al. (2009) observed a progressively decreasing trend in the SiO_2 composition of the eruptive products during the second phase of the eruption. The abrupt transition from basalt/basaltic-andesite (51 to 54 wt % SiO2) erupted in the first phase to trachyandisite and dacite (60 to 65 wt % SiO2) during the second phase, and the progressive decrease in SiO_2 during the second phase, have been attributed to a combination of both magma mixing and fractional crystallization (Kratzmann et al. 2009).

Soil and sediment sections exposed in river and road cuts, as well as in excavated trenches, located to the east and the southeast of the Hudson volcanic center, preserve pyroclastic fallout deposits that were derived from nine Holocene explosive eruptions of the Hudson Volcano, including two very large ones (Naranjo and Stern 1998). The younger of the two large events (H2) occurred at approximately 3,920 cal yrs BP and the older (H1) eruption occurred approximately 7,750 cal yrs BP (Stern 2008; Prieto et al. 2013). Based on the isopach maps for tephra from these eruptions, Naranjo and Stern (1998) determined that both the H1 and H2 eruptions generated greater volumes of ejected material than either the H3 eruption in 1991 or the 1932 Quizapu eruption (9.5 km^3; Hildreth and Drake 1992). Using radiocarbon age constraints and petrochemical data, Stern (1991, 2008) suggested that grey-green tephra layers in southernmost Patagonia, originally termed Tephra II by Auer (1974), are distal deposits of the H1 eruption derived from Hudson. These form >10 cm thick tephra deposits in Tierra del Fuego, and this eruption may have had a significant impact on the pre-historic people living on this island (Prieto et al. 2013). Based on the proximal and distal maximum isopachs for the H1 tephra, Stern (1991, 2008) estimated that this eruption possibly ejected >18 km^3 of material. The

chronology established by Naranjo and Stern (1998) shows that the recurrence interval between explosive eruptions of Hudson is irregular, but that the three largest Holocene explosive events (H1, H2, and H3 in 1991 AD) are relatively regularly spaced at 3,870 ± 40 years.

Although Naranjo and Stern (1998) did not observe any early Holocene or late-glacial tephra, Haberle and Lumley (1998) documented two late-glacial tephra deposits in lake sediments on Peninsula Taitao, 150 km southwest of the volcano. Radiocarbon dating of these deposits yielded ages of 14,560 cal yrs BP for eruption HW1 and 13,890 cal yrs BP for eruption HW2 (Haberle and Lumley 1998). Deep-sea Pacific Ocean sediment core MD07-3088 collected offshore the Chonos–Taitao archipelago (southern Chile) contained tephra deposits spanning the glacial period up into the Holocene (20,000 cal yrs BP to 1,920 cal yrs BP) and based on the major-element chemistry suggests that they were derived from the Hudson volcano (Carel et al. 2011).

Methods

Multiple sediment cores were obtained using a 5-cm-diameter modified Livingstone piston corer (Wright 1967), from small lakes within spatially limited water-shed basins selected to minimize the amount of inorganic sediment deposited in the lakes. X-ray images of the cores (Figs. 3 and 4) were taken to allow for better visible identification of the tephra deposits and to provide a means of stratigraphic correlation of the tephra layers between the cores. The white layers in these images are the denser lithologies, often tephra deposits, and the darker layers are the less dense organic-rich lacustrine sediments. The stratigraphic position of the Ho tephra layer, combined with several other key marker tephra deposits which were identified in the other cores, allowed for correlation of this deposit within the cores. The chronology of the tephra in the cores is controlled by AMS radiocarbon dates of organic material in the sediments (Table 1;

Miranda et al. 2013) and chronostratigraphic correlation of tephra layers. Radiocarbon dates were converted to calendar years before present (cal yrs BP) using the CALIB 5.01 program (Stuiver et al. 1998).

Once identified, the individual tephra deposits were extracted from the cores by removing approximately half of the deposit with a knife. Several of the Ho tephra layers were sufficiently large to sample at discrete 10 cm intervals to assess if any vertical stratification was present within the deposits. The tephra samples were washed to remove any organic matter, and then dried and sieved to remove any coarse fraction material not volcanic in origin. Within the Ho deposits, several different eruptive phases were apparent based on particle color and morphology. Based on these characteristics, the different phases were hand-picked out of the deposit. After cleaning, the bulk tephra samples and hand-picked components were mounted on petrographic slides to examine under a petrographic microscope in order to identify petrographic characteristics such as tephra morphology and the identity of mineral phases.

Trace-element data for both bulk tephra samples, hand-picked pumice, and dense glass fragments were determined using an ELAN D CR ICP-MS. Repeat analysis of a blind rock standard from Valmont Dike, Boulder CO demonstrates the reproducibility of the analyses (Fig. 1A; Table 1A in the Appendices). An independent analysis of Valmont Dike acquired from Act Labs (vmd control) is shown for comparison. For many of the elements, the vmd control is within the 2-sigma standard deviation of the average of the 19 repeat analyses. However, several elements, in particular the middle REE (Sm, Eu, Gd, Tb, and Dy) lie outside of the field defined by the 19 repeat analyses and are likely the result of analytical problems with the measurements (Fig. A1).

The major element compositions of pumice glass, dense glass, and mineral phases were determined using a Jeol JXA-733 Electron Microprobe. A 5-10 μm beam was used to obtain the analysis on the glass and mineral grains. The results from the volcanic glass are normalized to 100% anhydrous. The probe was operating at 15 KV accelerating potential with a 20 nA probe current. Larger beam widths and lower probe currents was used to minimize the loss of volatile elements for the high silica glasses. Sodium measurements are corrected to independent secondary standards obtained on pumice and glass of similar silica content from Hudson volcano to ensure accuracy of the reported analyses (Kratzmann et al. 2009, 2010).

Strontium isotopic ratios were measured using a Thermal Ionization Mass Spectrometer. Powdered samples were first dissolved in open containers in HF and $HC1O_3$. $^{87}Sr/^{86}Sr$ ratios were analyzed using Finnigan-MAT 261 four-collector static mass spectrometer. Replicate analyses of the SRM-987 standard in this mode yielded a mean $^{87}Sr/^{86}Sr$ of 0.71025± 2 (2σ). Measured $^{87}Sr/^{86}Sr$ were corrected to SRM-987=0.710299± 8. Errors of 2σ of the mean refer to the last two digits of the $^{87}Sr/^{86}Sr$ ratio. Details of the analytical procedure are outlined in Farmer et al. (1991).

CHAPTER II

TEPHRA DEPOSITS

General

The length of the sediment record for each lake is variable, but the lakes with Ho tephra contain sediments that date back to late-glacial time (~17,900 cal yrs BP; Miranda et al. 2013). These lake cores all preserve approximately 50 to >70 individual tephra layers derived from explosive eruptions of volcanoes in the area (Figs. 3 and 4; Table 2 in the Appendix). Based on their trace-element chemistry (Fig. 5) and their stratigraphic depth within the cores, specific source volcanoes for some of the Holocene eruptions have been identified (Figs. 3 and 4). These include the previously identified and dated large explosive eruption MAC1 of Maca at 1,440 cal yrs BP, H2 eruption of Hudson at ~3,920 cal yrs BP (Naranjo and Stern 1998), and MEN1 of Mentolat at 7,560 cal yrs BP (Naranjo and Stern 2004; Stern et al. 2013). Other chemically distinctive tephra from late-glacial eruptions that have not been previously described, such as a sequence of 10 thin tephra layers dated as <14,910 cal yrs BP (S10; Figs. 3 and 4), and a previously undocumented late-glacial Mentolat eruption (MENo), with chemistry, mineralogy and glass color and morphology similar to MEN1, are preserved in all or most of the cores and allow late-glacial strato-chronologic correlations between the cores.

Ho Deposits

Sixteen cores from the seven lakes studied contain an unusually thick tephra deposit, which provides evidence of a very large late-glacial eruption. Based on their bulk trace-element composition (Fig. 5), discussed in more detail below (Chapter III), and their spatial distribution (Fig. 6), these deposits were derived from a large late-glacial eruption of the Hudson volcano. I term this eruption Ho (Weller et al. 2013). In three cores from Lago Quijada, the closest to the

Hudson volcano (Fig. 2), the Ho layers range from 78 to 88 cm in thickness (Table 2). In ten of the eleven cores from five other lakes, all ≥100 km northeast of the Hudson volcano, the Ho tephra layers range between 50 to 70 cm in thickness (Fig. 5; Table 2). Only in one of the cores from Lago Toro is Ho less than 50 cm thick (Table 2). Pumice size was not systematically measured in any of the cores, but the bulk samples obtained from the Lago Mellizas core for petrochemistry contain Ho pumice grains with ≥2 cm maximum diameter. In a core from the seventh lake, Lago Élida (Figs. 1 and 2), more to the east of Hudson, and southeast of the other cores, Ho is only 14 cm thick (Fig. 4; Table 2) and all pumice grains are <1 cm in maximum diameter. In another core from Lago Shaman (LS; Fig. 1) more than 200 km to the northeast, a 2 cm thick late-glacial tephra (tephra V), one among 26 tephra identified in this core (de Porras et al. 2012), has tephra color, morphology, and chemistry (Fig. 5; Table 3 in the Appendix) similar to Ho.

Both compaction and/or thickening of tephra fall deposits may occur in lake sediments section. However, fifteen of the cores from the lakes that contain Ho tephra also contain layers of H2 tephra that are similar in thickness to the regionally mapped isopachs for this tephra (Table 2; Naranjo and Stern 1998), suggesting that thickening was not a problem for this younger tephra in these small lake basins. Based on this, as well as the lack of evidence for mixing of other sediment types within the Ho layers and the consistency of the thickness of the Ho layers both in different cores taken from different locations and depths in individual lakes and among the different lakes, I conclude that the Ho layers in these lakes have also not been significantly thickened compared to the original depositional thickness.

Tentative 50 cm and 10 cm tephra isopachs for the Ho eruption are presented in Figure 6, and compared to the 50 cm and the 10 cm tephra isopachs from the H1 eruption (Naranjo and

Stern 1998). The area of these isopachs (Fig. 7) indicates that the late-glacial Ho eruption was larger than any of the other younger explosive eruptions of Hudson (H1, H2 or H3 in 1991 AD), and I estimate its tephra volume as >20 km^3.

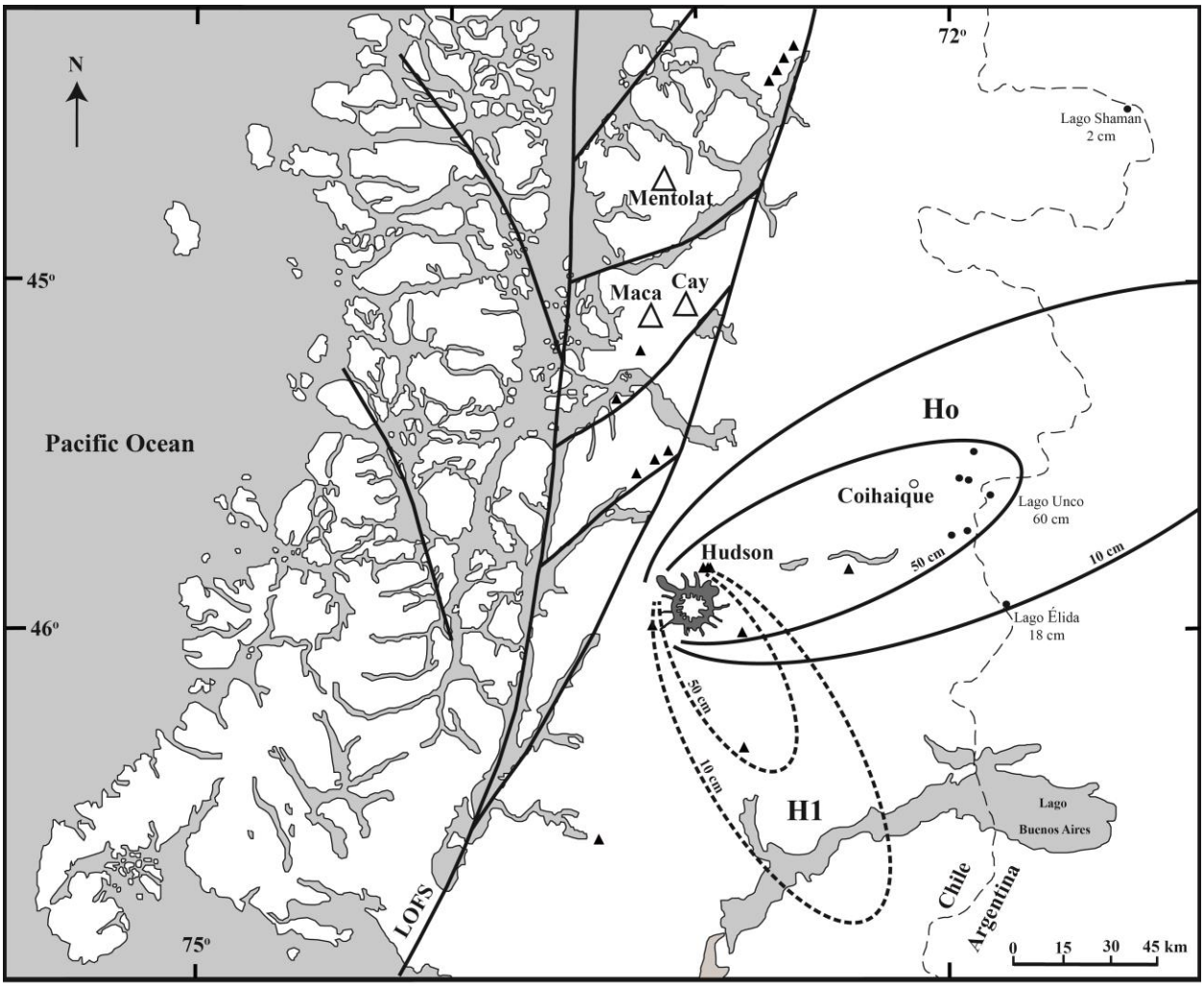

Figure 6. Estimated 50 and 10 cm isopachs of the Ho eruption (solid lines) compared to those of the mid-Holocene H1 eruption (dashed lines; Naranjo and Stern 1998). The distribution of the Ho tephra indicates a NE dispersion pattern.

The Ho tephra layer has been constrained in age in the cores using ^{14}C methods to date organic matter located in sedimentary layers just above and below this tephra (Table 1; Miranda et al. 2013). This provides an age for this eruption of between 17,300 and 17,440 cal yrs BP.

This age range is consistent with its stratigraphic position relative to other dated tephra in these cores (Fig. 3). Late-glacial tephra HW1 (14,560 cal yrs BP) and HW2 (13,890 cal yrs BP) documented by Haberle and Lumley (1998) from the Taitao Peninsula to the southwest of the Hudson volcano appear to be too young to be distal Ho tephra, and also occur in the opposite direction of the northeastern dispersal direction of Ho (Fig. 6). However, tephra TL6 at 870 cm depth from the Pacific Ocean sediment core is dated to 17,350 cal yrs BP likely was deposited from the same eruption responsible for the Ho deposit east of the volcanic arc. Furthermore, Markgraf et al. (2007) observed a 42 cm thick tephra between 1109 and 1151 cm depth from a core taken from Mallín Pollux (Fig. 2) which also likely corresponds to the Ho deposit.

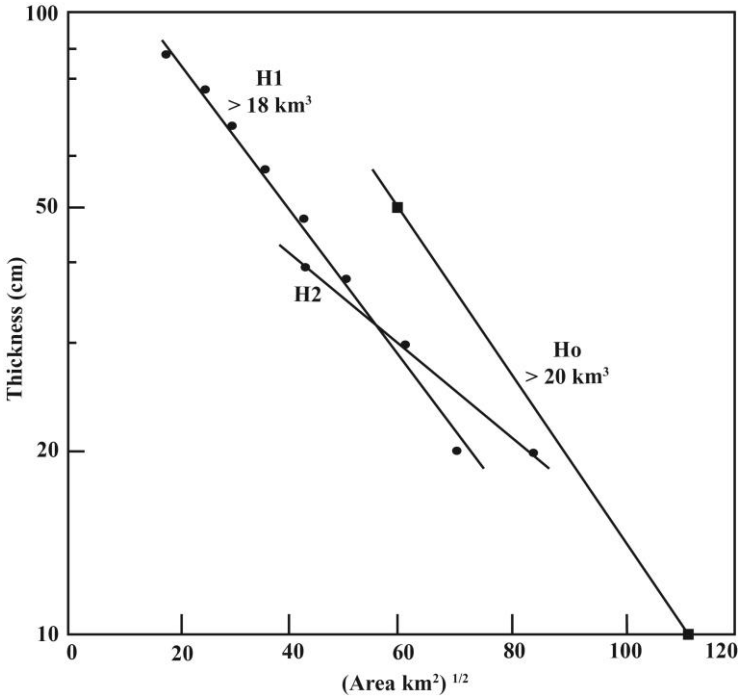

Figure 7. Estimated relative volumes from the H1, H2 (Naranjo and Stern 1998) and Ho eruptions.

Tephra Redistribution

One of the key factors in using tephra as a stratigraphic time marker and correlation tool is to determine if the deposit represents an in situ primary air fall deposit or if the deposit has

been reworked. After deposition of a tephra, eolian processes can completely strip a deposit from the terrain and remove any evidence of the volcanic eruption. However, when tephras are deposited in lacustrine environments, the volcaniclastic material settles out of suspension and preserves a record of the volcanic event.

Post deposition eolian and fluvial reworking can redistribute tephra from the land and transport the material into the lacustrine environment. Additionally, erosional episodes shortly after and several decades after the original tephra deposition can be remobilized and transported to lacustrine environments (Boygle, 1999).

Internal lake processes are additional mechanism which can redistribute tephra within lacustrine systems. Winnowing and focusing of tephra deposits by currents within lakes can cause post-depositional modification of the tephra deposits. Seismic activity can also cause slumping within the basins which would focus the sediments into the bathymetric lows in the lakes. All of these processes can modify an air fall tephra deposit within a lacustrine environment after deposition. However, it is unlikely that the Ho deposit has experience significant modification since the original deposition as evidenced by the consistent thickness of the deposit observed from multiple cores taken from the same lakes and the thickness of the deposits amongst the different lakes, the absence of clastic lacustrine sediments intermixed with the volcanic material, and the consistent thickness of the H2 deposit with regionally mapped isopachs (Naranjo and Stern 1998).

CHAPTER III

CHEMISTRY

Bulk tephra chemistry

All of the bulk tephra trace-element analyses from the Ho deposits (Table 3 in the Appendix) are similar to each other and occupy a narrow range of trace element chemistry characteristic of samples of lavas, pumice, and bulk tephra from other eruptions of the Hudson volcano (Fig. 5). The Ho bulk tephra trace-element analyses have elevated concentrations of Ti (>7000 ppm), Rb (>30 ppm), Zr (>200 ppm), Nb (>12 ppm), Y (>30 ppm), Ba (>500 ppm), La (>30 ppm) and Yb (>4 ppm) relative to both more mafic and felsic eruptions from other volcanoes in the region (Figs. 8 and 9; Stern 2001, 2008; Naranjo and Stern 1998). Primitive mantle normalized plots of incompatible trace elements and REE plots show the overall enrichment of LILE, HFSE and LREE for the bulk Ho samples (Fig. 9).

Tephra components

Glass and bulk compositions

The Ho tephra layers contain a diversity of glass particle morphologies and color that were produced by the Ho eruption (Fig. 10). The different components identified include dark grey to light tan glassy vesicle-rich pumice, denser dark black but vesicle-poor glassy fragments with a blocky morphology, and isolated mineral grains. The different phases of the tephra are randomly mixed within the deposit, which does not exhibit any vertical stratification in size or color of these components. This may be due in part to the deposition of these layers in lakes rather than as primary fallout deposits.

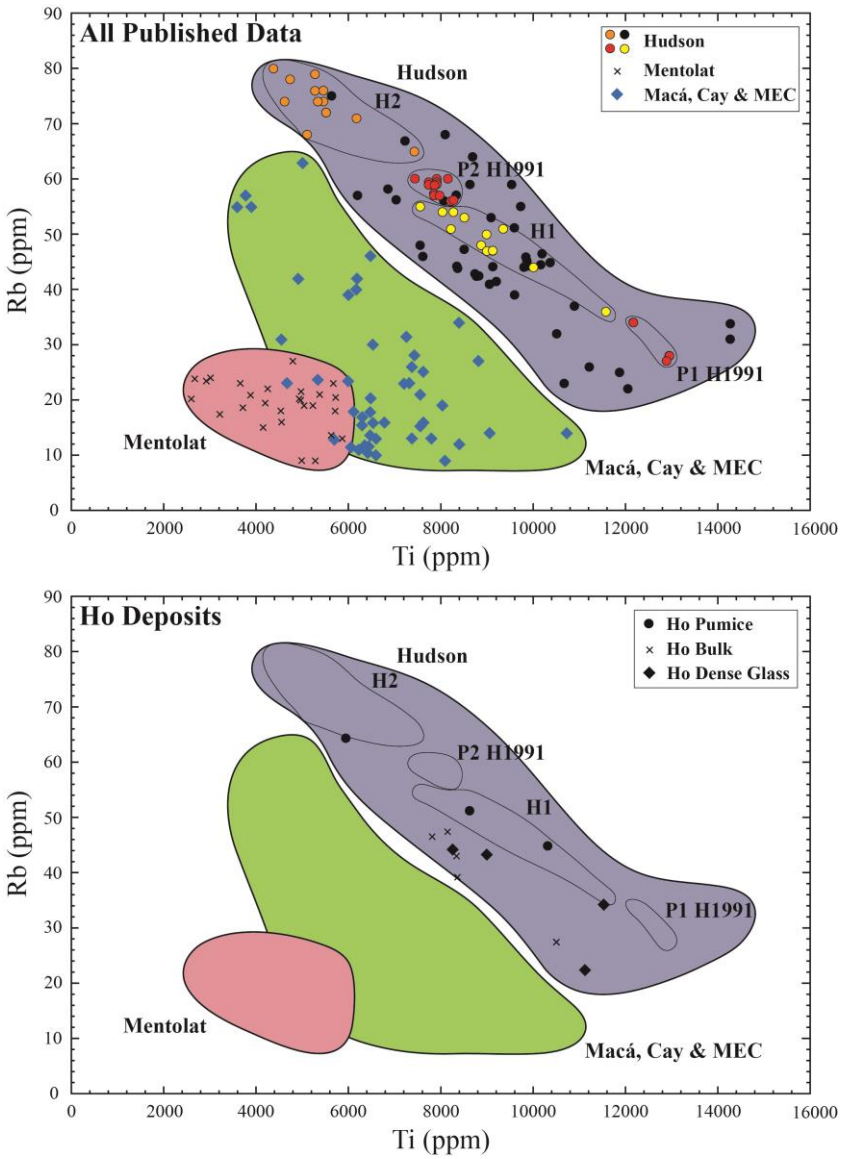

Figure 8. a) Ti versus Rb concentrations, in parts-per-million (ppm), for published data of lavas and tephras from Hudson, Mentolat, Macá, Cay and MEC (Futa and Stern 1988; López-Escobar et al. 1993; 1995; Naranjo and Stern 1998, 2004; D'Orazio et al. 2003; Gutiérrez et al. 2005, Kratzmann et al. 2009,2010), bulk tephra and hand-picked components from this study. Within the Hudson field, subfields for the H2, H1, P1 and P2 of the H3 1991 eruption of Hudson are shown. Hudson volcanic products have elevated concentrations of Rb and Ti compared to the products derived from other SSVZ volcanic centers.

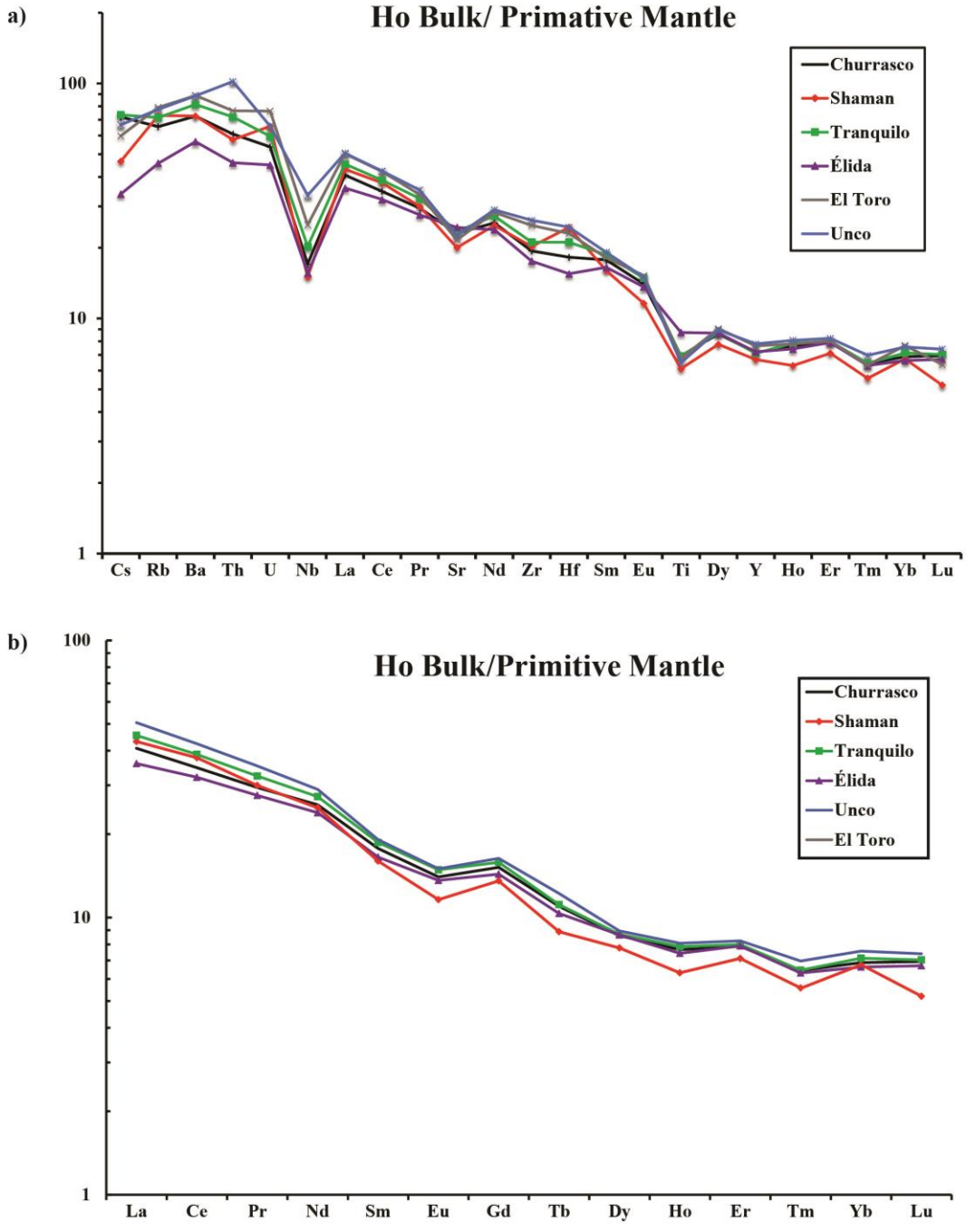

Figure 9. a) Primitive mantle-normalized trace-element diagram and b) primitive mantle-normalized REE plot for Ho bulk tephra samples (normalization factors are taken from McDonough and Sun (1995)). Overall, only minor deviations from the trend in a) and an overall LREE enriched trend is visible for all samples. Normalization factors P through Zr in ppm and Nb to U in ppb. P=90; K=240; Ti=1,205: Rb=0.600; Sr=19.9; Y=4.30; Zr=10.5; Nb=658; Cs=21; Ba=6,600; La=648; Ce=1,675; Pr=254; Nd=1,250; Sm=406 ; Eu=154; Gd=544; Tb=99; Dy=674; Ho=149 ; Er=438; Tm=68; Yb=441; Lu=67.5; Hf=283; Th=79.5; U=20.3.

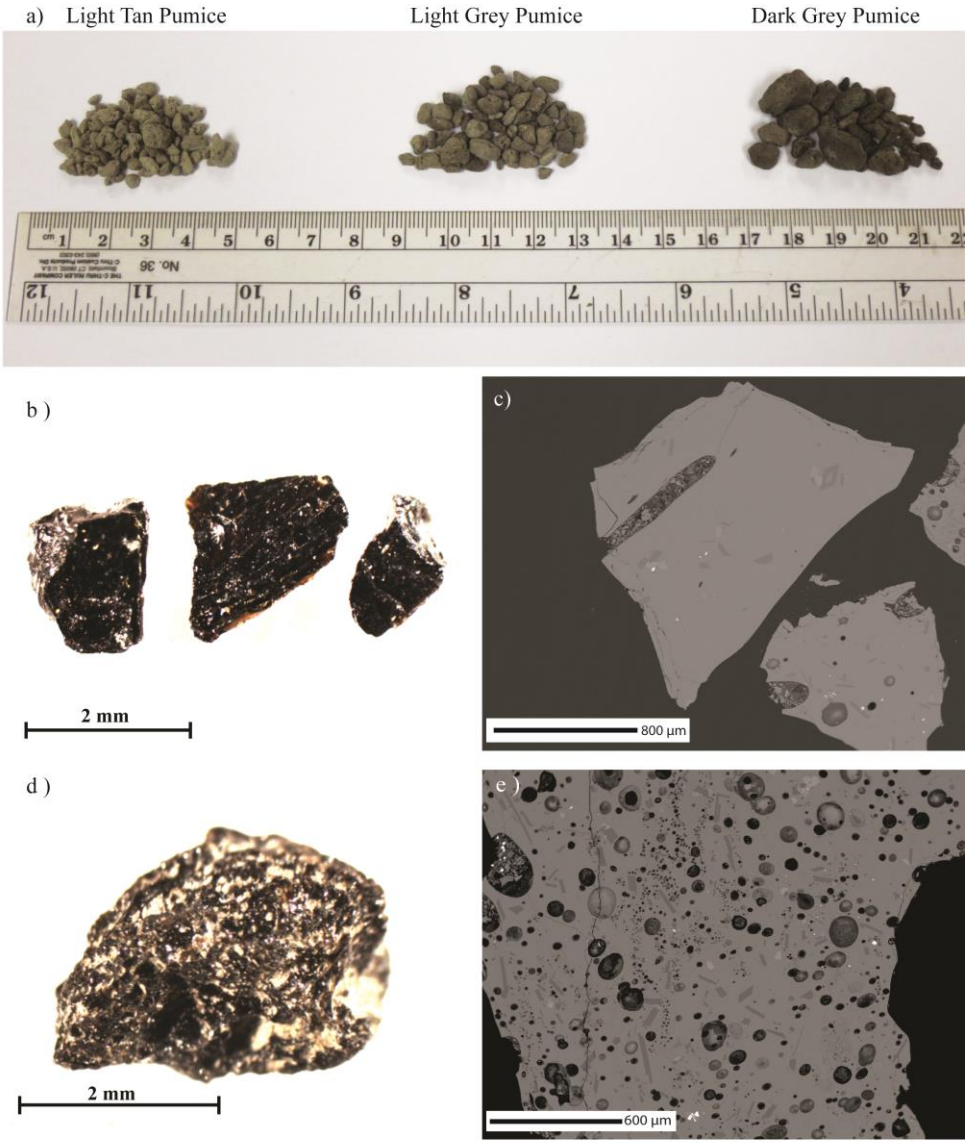

Figure 10. Images of the different components identified in the Ho tephra deposit. A) the three different color pumice groups selected from the deposit. The light tan pumice contains ~66 wt% SiO_2 while the lighter and dark grey pumice contain 59.3 % SiO_2 and 57.7% SiO_2, respectively (Table 4). B) and D) are images of the non-vesiculated and vesiculated dense dark glassy material. C) and E) are back-scattering electron image of the non-vesicualted dense black glass with few mineral microlites and the more micorlite-rich vesiculated dark glassy material, respectively. Within C) and E) the dark grey lath shaped microlites are feldspars, the light grey microlites are ferromagnesian minerals such as olivine and clinopyroxene and the white microlites are ilmenite.

The dense blocky black glass fragments themselves have a diversity of morphologies and textures, including fragments which contain few vesicles and few mineral microlites (Fig. 10), as

well as fragments with higher abundances of spherical vesicles and olivine, plagioclase, and clinopyroxene microlites, along with minor ilmenite. These blocky dark glassy fragments are the most mafic phase from the Ho eruption (Table 4 in the Appendix; Fig. 11), with an average glass composition of 55 wt % SiO_2, and higher Ti, Mn and Sr, and lower REE (Fig. 12), Rb, Ba and Zr contents, and higher Dy/Yb ratios (Fig. 13), then any pumice grains. The Ho components span nearly the entire compositional field of Hudson products with respect to Ti and Rb (Fig. 8).

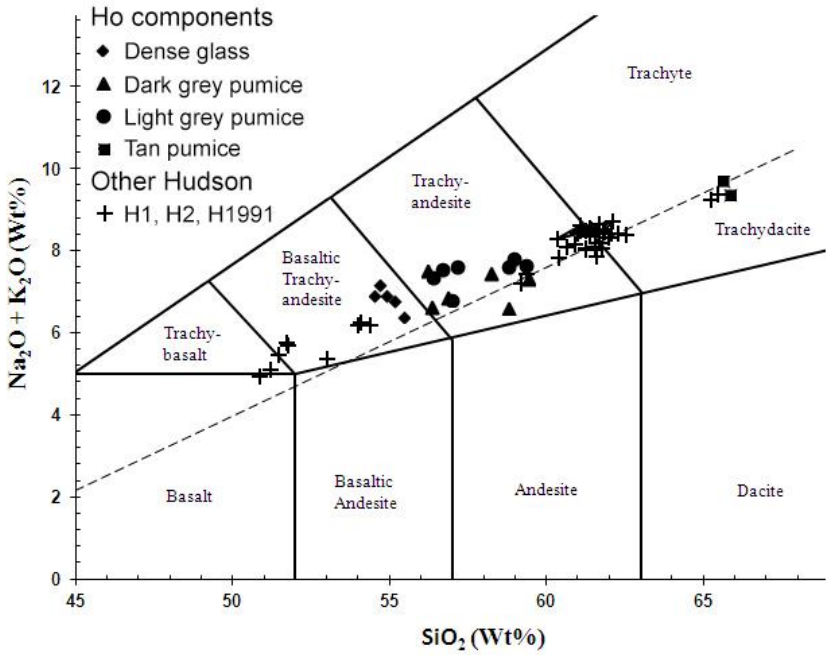

Figure 11. Total alkali content versus silica diagram, modified after Irvine and Baragaar (1971), showing the range of compositions of the Ho tephra glasses. The squares represent the light-tan pumice, the circles represent the light-grey pumice, the triangles represent the dark-grey pumice, the diamonds represent the dark glassy vesicle-poor material in the Ho deposits, and the plusses represent glass from other Hudson eruptive products (Futa and Stern 1988; Naranjo and Stern 1998; Gutiérrez et al. 2005, Kratzmann et al. 2009, 2010).

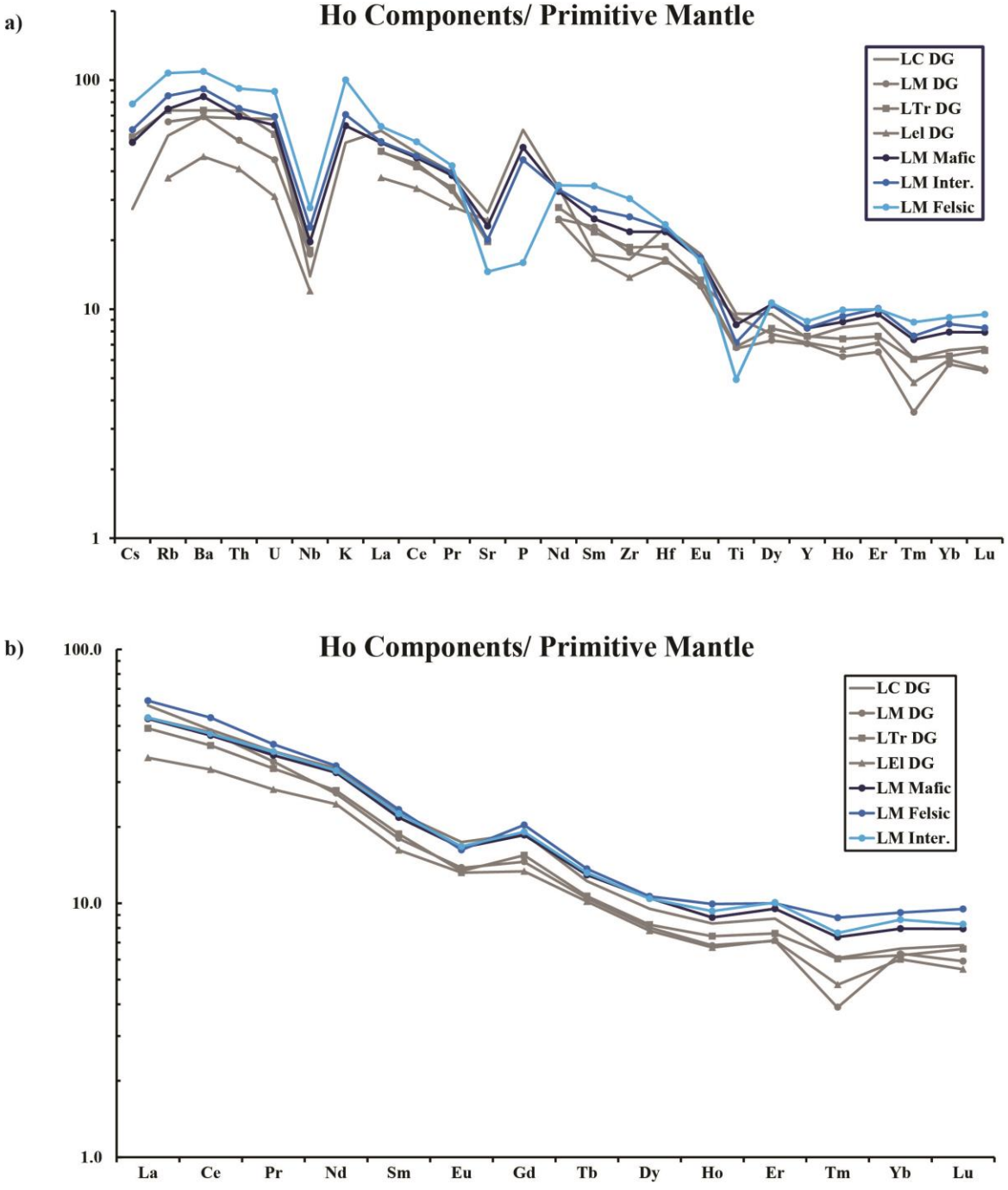

Figure 12. a) Primitive mantle-normalized trace-element diagram and b) primitive mantle-normalized REE plot for the Ho components (Normalization factors are taken from McDonough and Sun (1995)). An overall LREE enriched trend is visible for all samples in b). Normalization factors P through Zr in ppm and Nb to U in ppb. P=90; K=240; Ti=1,205: Rb=0.600; Sr=19.9; Y=4.30; Zr=10.5; Nb=658; Cs=21; Ba=6,600; La=648; Ce=1,675; Pr=254; Nd=1,250; Sm=406 ; Eu=154; Gd=544; Tb=99; Dy=674; Ho=149 ; Er=438; Tm=68; Yb=441; Lu=67.5; Hf=283; Th=79.5; U=20.3.

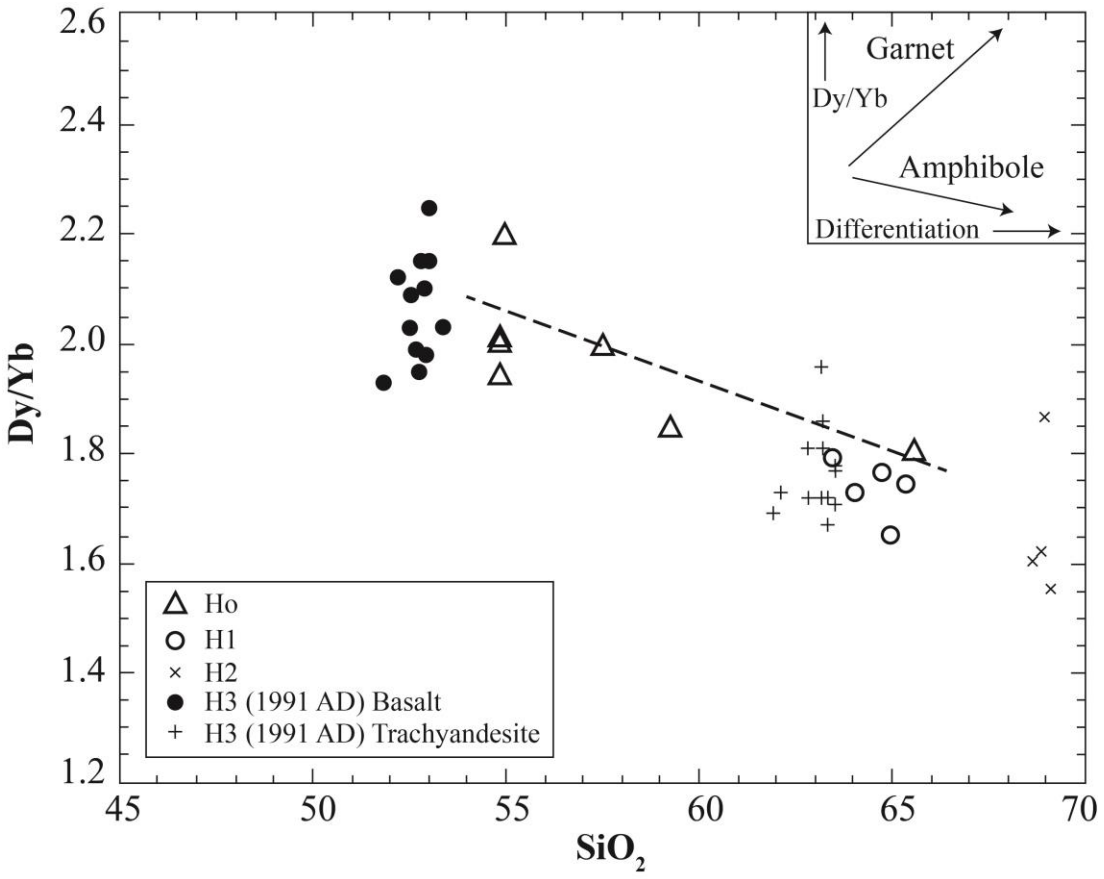

Figure 13. Dy/Yb concentration ratios of bulk Ho components versus their glass SiO2 contents (table 4) compared to the compositions of H1, H2, H3 glasses plotted by Kratzmann et al. (2010). The dashed line from the average phase 1 basalt erupted from the 1991, through the average Ho dense glass basaltic andesite to the Ho trachydacite pumice illustrates a small decrease in Dy/Yb with increasing SiO2, indicative of amphibole fractionation as shown in the inset (Davidson et al. 2007), although amphibole does not occur in any of the Hudson products.

The small glassy pumice fragments prepared for microprobe analysis contain few or no mineral grains, or these grains were possibly plucked out during the polishing processes. The pumice within the Ho tephra deposit range in color from dark grey to light tan. Three separate groups were identified and hand-picked from the tephra deposits: dark grey, lighter grey, and light tan (Fig. 10). The glass in the dark and lighter grey pumice groups ranges only between 57.7 to 59.3 wt % SiO_2 (Fig. 11; Table 4) despite their distinct color differences. Although the

distinction between the major element chemistries between the glasses in the two grey pumice groups is minor, the bulk-pumice trace element abundances show clear differences between the two components groups, with the lighter grey phase having lower Ti, Mn, and Sr and higher REE (Fig. 12), Rb, Ba and Zr contents, and lower Dy/Yb ratios (Fig. 13), than the dark-grey pumice. The lightest tan colored pumice is volumetrically less significant than the darker components and has an average silica content of 66 wt % SiO_2 (Fig. 11). Thus, nearly the entire range of compositional diversity observed in the H3 Hudson eruption of 1991 AD (Kratzmann et al. 2009) is also present in the Ho tephra, and a similar compositional gap as seen in the 1991 eruption is also present in the Ho eruption. However, the compositional gap between the dark and lighter colored pumice components, which corresponds to ~7 wt % between 59 to 66 wt % SiO_2 occurs at a higher silica content than the gap in SiO_2 content in the H3 Hudson eruption in 1991 AD, which occurs between 54 to 60 wt % SiO_2.

Figure 11 plots total alkali content versus silica, showing the compositional classification of the glass in the various components of the Ho eruption. Included in this diagram are Phase 1 and Phase 2 from the H3 eruption in 1991 AD (Kratzmann et al. 2009) and other Hudson volcanic products (Gutiérrez et al. 2005). The glasses from the Ho eruption range in composition from basaltic-trachyandesite to trachydacite which is characteristic of rocks and tephra derived from the Hudson volcano (Naranjo and Stern 1998; Gutiérrez et al. 2005). The Ho products are high K_2O rocks which straddle the curve dividing the alkaline and subalkaline fields described by Irvine and Baragaar (1971).

The light colored felsic pumice has an $^{86}Sr/^{87}Sr$ ratio of 0.70445 and the more mafic vesicle-poor dark glassy material has a ratio of 0.70447 (Table 5 in the Appendix). These isotopic compositions are very similar and coincide with strontium isotopic ratios measured on

all tephra and effusive rock samples from previous Hudson eruptions, which overall range in composition from 51 to 66 wt % SiO_2, and 525 to 227 ppm Sr as determined by ICP-MS analysis (Fig. 14; Futa and Stern 1988; Stern 1991, 2008; Naranjo and Stern 1998).

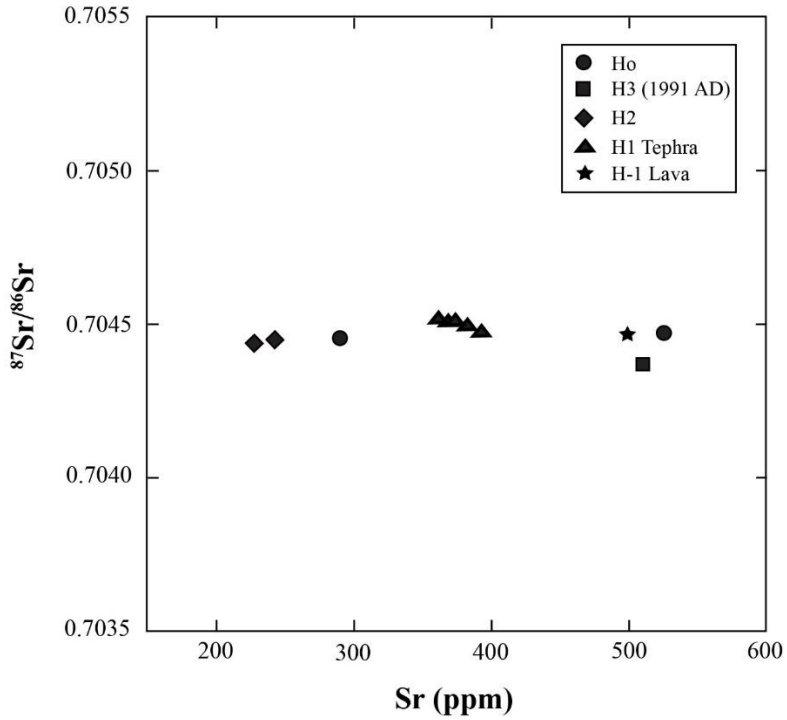

Figure 14. $^{87}Sr/^{86}Sr$ ratios versus Sr content for components from the Ho eruption (circles; Table 5), and bulk rock samples from Phases 1 and 2 of H3 in 1991 AD (square), H1 (triangles), H2 (diamonds) eruptions (Naranjo and Stern 1998; Stern 1991, 2008), and a basaltic andesite lava sample H-1 from the base of the volcano (Futa and Stern 1988).

Mineral Chemistry

Olivine microlites analyzed from the most mafic dark glassy fragments were generally anhedral to subhedral and are aggregated with microlites of clinopyroxene, plagioclase and Fe/Ti oxides. The analyzed olivine grains occupy a narrow compositional range of Fo_{75} to Fo_{67}, with olivine microlites from Lago Élida (LÉl) being slightly less MgO rich (Fo70-67) than the olivines in the blocky black glass separates from Lago Mellizas (LM) and Lago Churasco (LC;

Table 6 in the Appendix; Fig. 15). Clinopyroxene microlites in the dark glassy material also have a restricted range of En48-41;Wo43-35;Fs20-16 and clinopyroxene phenocrysts, which occur as large grains with some attached glass, occupy a similar compositional range En49-46;Wo35-27;Fs23-19. Clinopyroxenes from LÉl are similar to those analyzed in both LM and LC (Table 6, Fig. 15). Olivine and clinopyroxene microclites observed in the fallout deposits from the H3 1991 AD eruption and other Hudson eruptive products share similar chemistries to the mineral phases observed in Ho.

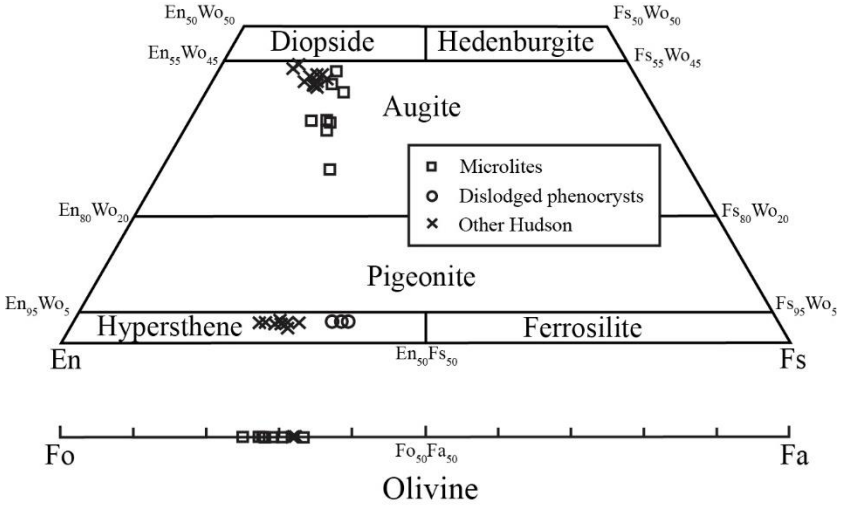

Figure 15. Wo-En-Fs classification diagram for pyroxenes and olivines. Clinopyroxene and olivines were present as microlites in dense black glassy fragments, while the orthopyroxene and some clinopyroxenes occur as large dislodged phenocrysts with some adhering glass.

No orthopyroxene microlites are observed within the blocky glass fragments or pumice, but they were found as large isolated grains mixed within the bulk tephra deposits. The majority of these crystals are elongated euhedral grains with some adhering glass. These crystals have a restricted compositional range between En59-61;Wo4-3;Fs38-36 (Table 6; Fig. 15). Orthopyroxene also occurs in H1 and H2 deposits, and was reported as well in trace amounts from the H3 tephra (Kratzmann et al. 2009).

Plagioclase occurs both as microlites contained within the dark blocky mafic glass fragment and also as larger phenocrysts, which, like orthopyroxenes, have become dislodged from the pumice and tephra in the bulk deposits, but still have glass adhering to their crystal surface. Plagioclase microlites within the black glassy fragments were generally euhedral to subhedral and they are the dominant microlite observed in this mafic component of the tephra deposit. These have a narrow compositional range of An51-58 (Table 7 in the Appendix, Fig. 16) with most of the grains being homogenous, with no core-to-rim variation. The larger plagioclase phenocrysts occupy a larger compositional range of An41-55 and also have no core-to-rim variation. Included in Figure 16 are plagioclase compositions from previous reports on Hudson volcanic products. These plagioclases span a wide range of compositions, with the largest population clustering near the composition of the plagioclase microlites and phenocrysts in the Ho tephra.

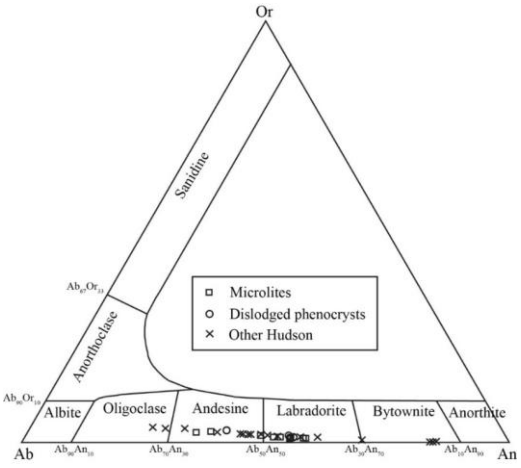

Figure 16. Ab-An-Or compositional triangle for feldspar microlites in dense dark glassy fragments and dislodged phenocryst.

CHAPTER IV

DISCUSSION

Hudson eruptive history

The distribution of the Ho tephra across the area indicates a northeast dispersion pattern of the ash fall with a maximum thickness of >85 cm at a distance of ~100 km from the source vent (Fig. 6). Based on comparison with all of the three previously documented large Holocene Hudson eruptions H1, H2 and H3 in 1991 AD (Stern 1991, 2008; Scasso et al. 1994; Naranjo and Stern 1998), Ho is larger, with an estimated volume of >20 km^3 (Fig. 7) of pyroclastic material. Considering a cylindrical depression of 300 m high with a radius of 5 km, Hudson's caldera has a volume of 23 km^3. Previous authors argued against the generation of this caldera from a single eruption due to insufficient eruption volume from any of the previously identified Holocene eruptions from Hudson (Gutiérrez et al. 2005). Instead, these authors supported the gradual formation of the caldera throughout the Holocene. However, these results indicate that the Ho eruption may have caused or initiated the incremental formation of the 10 km wide caldera on the Hudson volcano. This data suggest a sequential temporal decrease in the total volume of each large explosive eruption, from Ho >20 km^3, to H1 >18 km^3, to H2 and finally H3 in 1991 AD with only ≥4 km^3 (Fig. 17).

Adding the total estimated volumes of Ho along with the previously documented eruptions H1, H2 and H3 in 1991 AD, as well as other smaller eruptions indicated by tephra in these lake cores and other smaller eruptions from west of the volcanic arc (Fig. 17; Haberle and Lumley 1998; Carel et al. 2011), indicate that ≥45 km^3 of pyroclastic material has been erupted from Hudson in the last ~20,000 yrs (Fig. 17). This would make Hudson the most active volcano

in the southern Andes in terms of total volume of pyroclastic material erupted by explosive eruptions since the beginning of deglaciation at approximately 17,900 cal yrs BP.

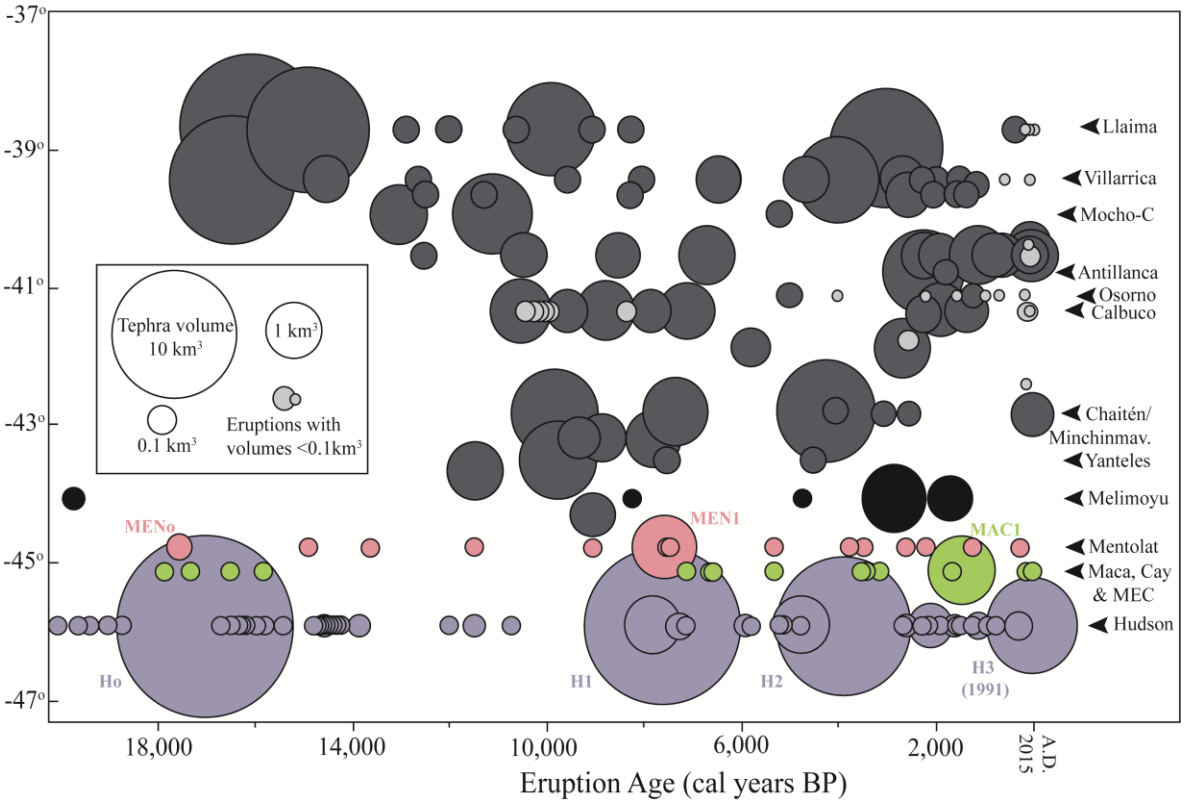

Figure 17. Volumes of explosive eruptions of different later-glacial and Holocene ages (cal yrs BP) from volcanoes in the southern SVZ between latitudes 39°S (Llaima) to 46°S (Hudson), modified from Watt et al. (2013) to include the large late-glacial Ho eruption from Hudson (>20 km^3), other smaller eruptions identified in the lake cores and glacial to late-glacial eruptions observed in Pacific core MD07-3088 (Carel et al. 2011). Hudson volcano, with four large explosive eruptions and numerous other smaller explosive events, totaling >45 km^3 volume over the last 17,500 yrs, has produced the greatest volume of explosive eruptive products in the SSVZ over this time period.

Petrogenesis

An interesting distinction between the Ho eruption and the H3 eruption in 1991 AD is the lack of stratification of the Ho deposits with regard to the size or composition of the distinct components in the deposit, even though both eruptions contain bimodal eruptive products. The H3 eruption in 1991 had a clear temporal distinction between the two chemically different phases

as the eruption evolved from basalt and basaltic andesite in Phase 1 to trachydacite and andesite in Phase 2. The genetic relationship between the two phases has been attributed to a combination of magma mixing and fractional crystallization. Major and trace element modeling by Kratzmann et al. (2009) indicates that fractional crystallization of plagioclase (7.8-18.0%), clinopyroxene (4.8-11.6%), orthopyroxene (1.9-6.9%), magnetite (2.9-6.7%) and apatite (0.5-1.5%) from a mafic parental magma similar to the P1 basalt is capable of generating magma with a trachydacite composition similar to the dominant tephra observed in Phase 2. Kratzmann et al. (2010) subsequently presented similar fractional crystallization models, involving the anhydrous phases observed in the eruption products, for producing the H1 and H2 trachyandesites and trachydacites from a basalt similar to that erupted during Phase 1 of the H3 eruption in 1991 AD. However, they further suggested that trace-element concentrations and ratios, specifically decreasing Dy/Yb ratio trends through the sequence basalts, trachyandesites, and trachydacites erupted in these three eruptions (Fig. 13), could be better explained by amphibole fractionation from a basalt parent at >6 km depth (Davidson et al. 2007), followed by disappearance of amphibole, due to decreasing pressure and increasing temperature as these magmas rose toward the surface (Fig. 18). Ho components exhibit similar Dy/Yb ratio trends (Fig. 13) consistent with this latter cryptic amphibole fractionation model.

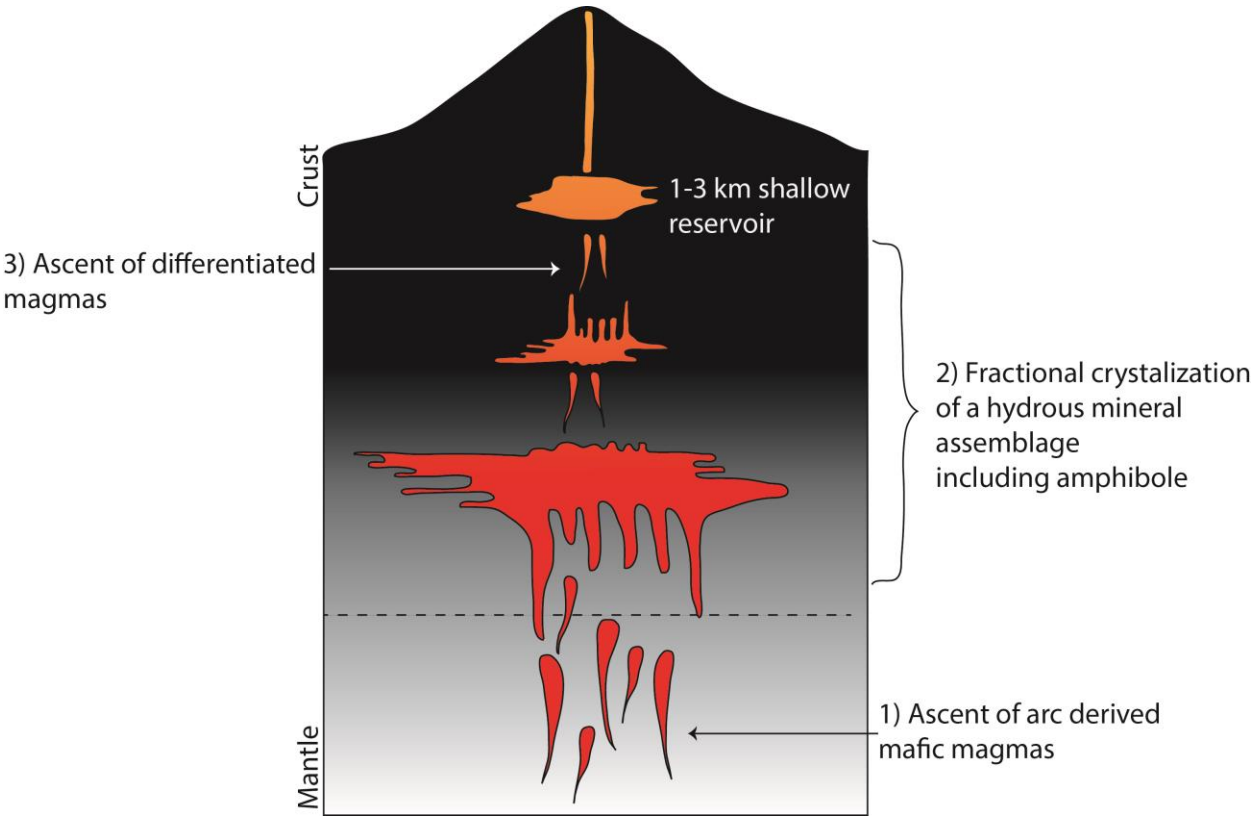

Figure 18. Model for the Holocene eruptions at Hudson volcano. 1) Slab dewatering and primary melt generation. 2) Mantle-derived mafic melts pond in the mid to lower crust (~6–24 km) where crystal fractionation involving a hydrous mineral assemblage that includes amphibole generates the more evolved compositions. 3) Derivative melts, now carrying the geochemical signature of amphibole, ascend and stall in the shallow crust where they undergo low-pressure fractionation via an anhydrous mineral assemblage prior to eruption (Modified from Kratzmann et al. 2010)

The strontium isotope ratios of the mafic dark glassy fragments and the felsic light tan pumice in the Ho tephra deposits, as well as all the other analyzed extrusive units from the Hudson volcano, which overall range in SiO_2 from 51 to 66 wt %, show almost no variation (Fig. 14; Table 5). Hudson's magmas ascend though the eastern portion of the Northern Patagonian Batholith that has been dated to approximately 100-120 Ma and on average, has a higher strontium isotopic composition than Hudson's eruptive products (Pankhurst et al. 1999). The homogenous isotopic composition between the different samples is consistent with the

suggestion of Kratzmann et al. (2009) that the evolution of Hudson magmas are controlled by fractional crystallization processes, and that crustal assimilation is not responsible for the generation of the more evolved phases observed in either the H3 eruption in 1991 or any of the other documented Hudson eruptions. It is likely that crystal-liquid fractionation process similar to those suggested by Kratzmann et al. (2009) for the H3 eruption controlled the evolution of the Ho eruptive products, which also range from basaltic-trachyandesite to trachydacite in composition.

The Ho deposits are overall dark in color, with a much greater abundance of mafic dark glass fragments and dark to light gray pumice compared to light tan felsic pumice. The bulk tephra trace element abundances (Table 3), which are a representative portion of each deposit, can also be used to evaluate the relative proportions of mafic or felsic components (Table 3) in this deposit. Based on the comparison of the bulk-tephra, dark glassy material, and the pumice chemical analysis, the composition of the whole tephra samples are more similar to the mafic dark glassy material, confirming that the eruption was predominantly mafic with only a smaller portion of felsic material. Thus, although Ho at ~17,400 cal yrs BP was bi-modal, it erupted a greater proportion of mafic compared to more felsic material. H1 at 7,750 cal yrs BP was essentially andesitic in composition (Naranjo and Stern 1998). H2 at 3,960 cal yrs BP was more felsic than H1, being composed essentially of dacite. H3 in 1991 AD was again bi-modal, but with a much smaller proportion of mafic compared to felsic material (Kratzmann et al. 2009). Thus, the large explosive eruptions of Hudson have evolved from more to progressively less mafic through late-glacial to historic times, and their volumes have decreased.

Sedimentation Rates

Using the radiocarbon ages of the S10 tephra (Fig. 3; Miranda et al. 2013) and previously dated eruptions (MAC1; H2; MEN1), a depth versus age sedimentation profile for the Lago Unco core is compared to profiles from other lakes in the region (Fig. 19), including Mallín Pollux (Markgraf et al. 2007) and Augusta (Villa-Martínez et al. 2012). The profile for the Lago Unco core near Coyhaique were constructed using the 1,440 cal yrs BP (670 AD) age of the MAC1 tephra determined by Naranjo and Stern (2004), rather than the 1,950 cal yrs BP (160 AD) age for this tephra (T3) determined by Elbert et al. (2013). When the age determination of Elbert et al. (2013) is used to construct the profiles, there is significant fluctuation of sedimentation rate, more rapid between 309 BC and 160 AD and much slower between 160 AD and 1100 AD (see Figure 2a in Elbert et al. 2013), while the rates are more constant when MAC1 tephra is assigned the age determined by Naranjo and Stern (2004). The previously described Mallín Pollux core (Markgraf et al. 2007), based on independent chronological data, does not show such fluctuations.

The profiles all exhibit intervals of both slower and more rapid accumulation of material within the lakes. Significantly, the cores show similar patterns, with relatively rapid sedimentation rates during Late Glacial times (18,000 to approximately 15,000 cal yrs BP), followed by relatively slower rates up to the mid-Holocene (15,000 to 7,500 cal yrs BP), after which relatively more rapid sedimentation rates prevail. However, significantly different explanations have been proposed to explain these changes in the Mallín Pollux (Markgraf et al. 2007) and Lago Augusta (Villa-Martínez et al. 2012) cores. Resolving these differences is beyond the scope of this thesis. Nevertheless the profiles illustrate the power of tephrochronology for constraining temporal correlations among lake core records over a

relatively large region, and the data suggest that these changes in sedimentation rates were produced by regional environmental changes that affected lakes both in the semi-arid region to the east of the current drainage divide (Unco), as well as in the wetter region more to the west (Mallín Pollux).

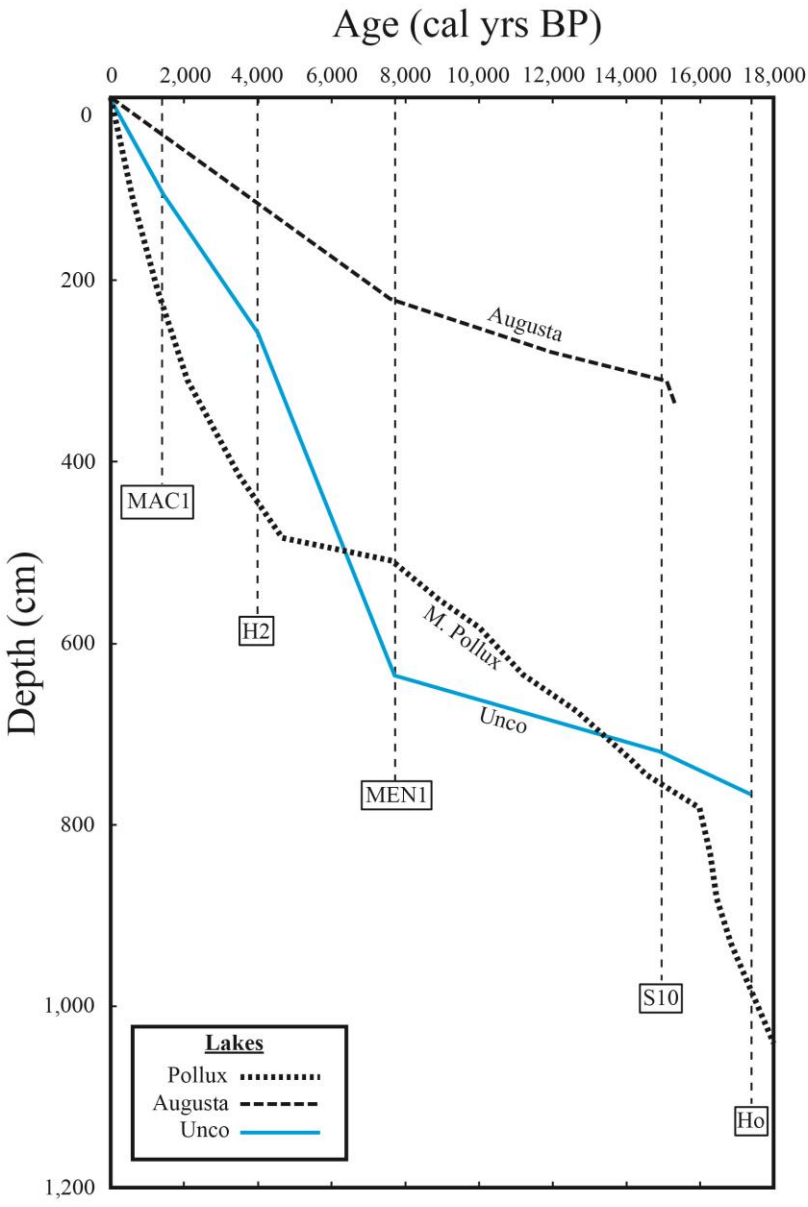

Figure 19. Sedimentation profiles for the Lago Unco lake core using the ages of previously dated large explosive eruptions from Hudson (H2), Mentolat (MEN1) and Macá (MAC1) (Naranjo and Stern 2004) including two profiles from Mallín Pollux (Markgraf et al. 2007) and Lago Augusta (Villa-Martínez et al. 2012).

BIBLIOGRAPHY

Auer V (l974) The isorythmicity subsequent to the Fuego-Patagonian and Fennoscandian ocean level transgressions and regressions of the latest glaciation. Ann Acad Sci Fenn (Helsinki), Ser A, III. Geol Geogr 115: 1–188

Best JL (l989) Fluidization pipes in volcaniclastic mass flows, Volcán Hudson, southern Chile. Terra Nova 1: 203–208

Best JL (l992) Sedimentology and event timing of a catastrophic volcaniclastic mass flow, Volcán Hudson, southern Chile. Bull Volcanol 54: 299–318

Cande SC, Leslie RB (1986) Late Cenozoic Tectonics of the Southern Chile Trench. J Geophys Res 91(B1): 471–496

Carel M, Siani G, Delpech G (2011) Tephrostratigrapy of a deep-sea sediment sequence off the south Chilean margin: New insight into the Hudson volcanic activity since the last glacial period. J Volcanol Geotherm Res. 208: 99-111

Cembrano J, Hervé F, Lavenu A (l996) The Liquiñe-Ofqui fault zone: long-lived intra-arc fault system in southern Chile. Tectonophys 259: 55–66

Cevo J (l978) Informe preliminar sobre erupción del Volcán Hudson norte o Volcán Huemules. Trapananda 1: 35–42

de Porras ME, Maldonado A, Abarzúa AM, Cárdenas ML, Francois JP, Martel-Cea A, Stern, CR (2012). Postglacial vegetation, fire and climate dynamics at Central Chilean Patagonia (Lake Shaman, 44°S). Quat Sci Revs 50: 71–85

D'Orazio M, Innocenti F, Manetti P, Tamponi M, Tonarini S, González-Ferrán O, Lahsen A (2003) The Quaternary calc-alkaline volcanism of the Patagonian Andes close to the

Chile triple junction: geochemistry and petrogenesis of volcanic rocks from the Cay and Maca volcanoes (~45°S, Chile). J of S Amer Earth Sci 16(4): 219–242

Davidson J, Turner S, Handley H, Macpherson C, Dosseto A (2007) Amphibole "sponge" in arc crust? Geology 35(9): 787-790

Elbert J, Wartenburg R, von Gunten L, Urrutia R, Fisher D, Fujak M, Hamann Y, Greber ND, Grosjean M (2013) Late Holocene air temperature variability reconstructed from the sediments of Laguna Escondida, Patagonia Chile. Palaeogeog Palaeoclimat Palaeoecol 396: 482-492

Farmer GL, Broxton DE, Warren RG, Pickthorn W (1991) Nd, Sr, and O isotopic variations in metaluminous ash-flow tuffs and related volcanic rocks at Timber Mountain/Oasis Valley Caldera, Complex, SW Nevada: implication for the origin and evolution of large-volume silicic magma bodies. Contrib Mineral Petrol 109: 53–68

Fuenzalida RP (1976) The Hudson volcano. Proceedings of the IAVCEI symposium on Andean and Antarctic volcanology problems, 1974, Santiago, Chile pp 78–87

Fuenzalida RP, Espinosa WN (1974) Hallazgo de una caldera volcánica en la provincia de Aisén. Rev Geol Chile 1: 64-66

Futa K, Stern CR (l988) Sr and Nd isotopic and trace element compositions of Quaternary volcanic centers of the southern Andes. Earth Planet Sci Lett 88: 253–262

Gutiérrez F, Gioncada A, Gonzalez-Ferran O, Lahsen A, Mazzuoli R (2005) The Hudson volcano and surrounding monogenetic centres (Chilean Patagonia): an example of volcanism associated with ridge-trench collision environment. J Volcanol Geotherm Res 145: 207–233

Haberle SG, Lumley SH (1998) Age and origin of tephras recorded in postglacial lake sediments to the west of the southern Andes, 44oS to 47oS. J Volcanol Geotherm Res. 84: 238-256

Hildreth W, Drake RE (l992) Volcán Quizapu, Chilean Andes. Bull Volcanol 54: 93–125

Irvine TN, Baragaar WRA (1971) A guide to the chemical classification of the common volcanic rocks. Can J Earth Sci 8(5): 523–548

Kratzmann DJ, Carey S, Scasso RA, Naranjo JA (2009) Compositional variations and magma mixing in the 1991 eruptions of Hudson volcano, Chile. Bull Volcanol 71(4): 419–439

Kratzmann DJ, Carey S, Scasso RA, Naranjo JA (2010) Role of cryptic amphibole crystallization in magma differentiation at Hudson volcano, Southern Volcanic Zone, Chile. Contrib Mineral Petrol 159: 237–264

López-Escobar L, Kilian R, Kempton P, Tagiri M (l993) Petrology and geochemistry of Quaternary rocks from the southern volcanic zone of the Andes between 41°30’ and 46°00’S, Chile. Rev Geol Chile 20: 33–55

Markgraf V, Whitlock C, Haberle S (2007) Vegetation and fire history during the last 18,000 cal yr B.P. in Southern Patagonia: Mallín Pollux, Coyhaique, Province Aisén (45°41'30", 71°50'30"W, 640 m elevation). Palaeogeogr Palaeoclimatol Palaeoecol 254: 492-507

McDonough WF, Sun SS, (1995) The composition of the Earth, Chem Geol 120: 223-253

Miranda CG, Moreno PI, Vilanova I, Villa-Martinez RP (2013) Glacial fluctuations in the Coyhaique-Balmaceda sector of central Patagonia (45oS-46oS) during the last glacial termination. Bollettino di Geofisica. 54: 268-271

Naranjo JA (l991) Nueva erupción del volcán Hudson. Rev Geol Chile 18: 183–184

Naranjo JA, Stern, CR (1998) Holocene explosive activity of Hudson Volcano, southern Andes. Bull Volcanol 59(4): 291–306

Naranjo JA, Stern CR (2004) Holocene tephrochronology of the southernmost part (42°30'-45°S) of the Andean Southern Volcanic Zone. Rev Geol Chile 31(2): 225–240

Nelson E, Forsythe R, Arit I (1994) Ridge collision tectonics in terrane development. J S Amer Earth Sci 7(3-4): 271–278

Pankhurst RJ, Weaver SD, Hervé F, Larrondo P (1999) Mesozoic–Cenozoic evolution of the North Patagonian Batholith in Aysén , southern Chile. J Geol Soc 156: 673–694

Prieto A, Stern CR, Esterves J (2013) The peopling of the Fuego-Patagonian fjords by littoral hunter-gatherers after the mid-Holocene H1 eruption of Hudson Volcano. Quat Internat 317: 3-13

Scasso RA, Corbella H, Tiberi P (l994) Sedimentological analysis of the tephra from the 12–15 August l991 eruption of Hudson volcano. Bull Volcanol 56: 121–132

Siani G, Colin C, Mechel E, Carel M, Richter T, Kissel C, Dewilde F (2010) Late Glacial to Holocene terrigenous sediment record in the Northern Patagonian margin: paleoclimate implications. Palaeogeogr Palaeoclimatol Palaeoecol 297: 26-36

Stern CR (l990) Tephrochronology of southernmost Patagonia. Natl Geogr Res 6: 110–126

Stern CR (l991) Mid-Holocene tephra on Tierra del Fuego (54°S) derived from the Hudson volcano (46oS): evidence for a large explosive eruption. Rev Geol Chile 18: 139–146

Stern CR (2004) Active Andean Volcanism: its geologic and tectonic setting. Rev Geol Chile 31(2): 161-206

Stern CR (2008) Holocene tephrochronology record of large explosive eruptions in the southernmost Patagonian Andes. Bull Volcanol 70(4): 435–454

Stern CR, Kilian R (l996) Role of the subducted slab, mantle wedge and continental crust in the generation of adakites from the Andean austral volcanic zone. Contrib Mineral Petrol 123: 263–281

Stern CR, Moreno H, López-Escobar L, Clavero JE, Lara LE, Naranjo JA, Parada MA, Skewes MA (2007) Chilean Volcanoes. Chapter 5 in "The Geology of Chile" (T Moreno & W. Gibbons, eds), Geologic Society of London, pp 149-180

Stern CR, Moreno PI, Henrique WI, Villa-Martinez RP, Sagredo E, Aravena JC (2013) Tehrochronolgy in the area around Cochrane, southern Chile. Bollettino di Geofisica 54: 199-202

Stuiver M, Reimer PJ, Braziunas TF (1998) High-precision radiocarbon age calibration for terrestrial and marine samples. Radiocarbon 40(3): 1127–1151

Tobar A (l972) Event 80–71. l971 Annual Report, Smithsonian Institution, Center of short-lived phenomena, pp 105–109

Vargas G, Rebolledo S, Sepúlveda SA, Lahsen A, Thiele R, Townley B, Padilla C, Rauld R, Herrera MJ, Lara M (2013) Submarine earthquake rupture, active faulting and volcanism along the major Liquiñe-Ofque Fault Zone and implications for seismic hazard assessment in the Patagonian Andes. Andean Geol 40: 141-171

Villa-Martínez R, Moreno PI, Valenzuela MA (2012) Deglacial and postglaical vegetation changes on the eastern slopes of the central Patagonian Andes (47oS). Quat Sci Rev 32: 86-99

Volker D, Kutterolf S, Wehrmann H (2011) Comparative mass balance of volcanic edifices at the southern volcanic zone of the Andes between 33oS and 46oS. J Volcanol Geotherm Res. 205: 114-129

Watt SFL, Pyle DM, Mather TA (2013) The volcanic response to deglaciation: evidence from glaciated arcs and a reassessment of global eruption records. Earth Sci Rev 122: 77-102

Weller DJ, Stern CR, Miranda CG, Moreno PI, Villa-Martinez RP (2013) A very large (>20km3) late-glacial eruption (Ho) of the Hudson volcaono, southern Chile. Bollettino di Geofisica 54: 203-206

Wilson T, Cole J, Johnston D, Cronin S, Stewart C, Dantas A (2012) Short-and long-term evacuation of people and livestock during a volcanic crisis: lessons from the 1991 eruption of Volcan Hudson, Chile. J Applied Volcanol 1: 2

Wilson T M, Cole JW, Stewart C, Cronin SJ, Johnston DM (2011) Ash storms: impacts of wind-remobilised volcanic ash on rural communities and agriculture following the 1991 Hudson eruption, southern Patagonia, Chile. Bull Volcanol 73: 223–239

Wright HE Jr, (1967) A square-rod piston sampler for lake sediments. J Sed Petrol 37: 975–976

APPENDIX A: Tables

Table 1. Radiocarbon age constraints on Ho tephra deposits in lake cores from near Coyhaique, Chile.

Site	Laboratory code	Core	Core depth (cm)	^{14}C yr BP	cal yr BP (range 2σ)	Median cal yr BP
<Ho						
Lago Espejo	CAMS-154865	PC1003AT8	1,193-1,194	13,080±30	15,221 - 16,402	15,818
Lago Unco	UCIAMS-122978	PC1103ET8	1,419-1,420	13,430±50	16,204 - 16,875	16,612
Lago Unco	CAMS-159614	PC1103ET8	1,423-1,424	13,720±45	16,692 - 17,018	16,850
Lago Mellizas	CAMS-159606	PC1106AT6	1,348-1,349	13,810±110	16,691 - 17,178	16,914
Lago Quijada	CAMS-159607	PC1001DT10	1,664-1,665	14,220±45	16,992 - 17,595	17,299
>Ho						
Lago Unco	CAMS-159613	PC1103ET9	1,517-1,518	14,345±45	17,132 - 17,788	17,443
Lago Mellizas	UCIAMS-122999	PC1106BT7	1,452-1,453	14,670±45	17,573 - 18,368	17,847
Lago Quijada	CAMS-154860	PC1001ET9	1,685-1,686	14,735±30	17,648 - 18,432	17,920
Lago Mellizas	UCIAMS-123030	PC1106BT7	1,457-1,458	14,800±90	17,661 - 18,509	18,014

Table 2. Thicknesses in cm of the Ho and H2 tephra deposits in the cores from the seven lakes near Coyhaique, Chile

		Ho			H2			
Lake	Core	Thickness (cm)	Top (cm)	Bottom (cm)	Thickness (cm)	Top (cm)	Bottom (cm)	Isopach (cm)
Quijada	PC1001A	78	T3 95	T4 73	-	-	-	-
	PC1001B	85	T3 45	T4 30	-	-	-	-
	PC1001C	deformed	-	-	20	T2 15	T2 35	20
	PC1001D	88	T10 50	T11 38	20	T2 60	T2 78	20
Churrasco	PC1201A	65	T6 5	T6 70	18	T2 10	T2 28	20
	PC1201B	60	T6 60	T7 20	18	T1 60	T1 68	20
Unco	PC1103D	60	T8 30	T8 90	12	T3 10	T3 22	10
	PC1103E	60	T8 78	T9 38	10	T3 58	T3 68	10
Mellizas	PC1106A	68	T7 0	T7 68	10	T2 95	T3 5	10
	PC1106B	60	T6 60	T7 20	10	T2 55	T2 65	-
Toro	PC1002B	50	T6 95	T7 45	10	T3 0	T3 10	10
	PC1002C	35	T8 20	T8 55	7	T3 18	T3 25	10
Tranquilo	PC1203A	65	T11 75	T12 40	10	T5 0	T5 10	>5
	PC1203B	60	T10 75	T11 35	9	T4 35	T4 44	>5
	PC1203C	70	T5 0	T5 70	6	T2 42	T2 48	>5
	PC1203D	68	T4 70	T5 38	7	T2 11	T2 18	>5
Élida	PC1105B	18	T7 16	T7 28	12	T1 56	T1 68	10

*isopach thickness for H2 from Naranjo and Stern (1998).

Table 3. Bulk tephra trace-element compositions (in ppm) of bulk samples of Ho

Lake	LC	LTr	LU	LT	LEl	LS
Section	AT6	AT12	ET9	BT7	BT7	AT
Depth (cm)	67-74	0-40	0-3	34-37	10-28	
n	3	5	1	3	3	1
Phase	Bulk	Bulk	Bulk	Bulk	Bulk	Bulk
Ti	8365	8346	7810	8150	10508	7366
V	240	212	175	187	309	-
Cr	15	21	17	13	34	-
Mn	1182	1157	1097	1161	1260	890
Co	29	30	26	48	47	-
Ni	18	21	13	35	29	-
Cu	69	51	67	30	68	-
Zn	112	109	114	119	108	-
Rb	39	43	47	47	27	44
Sr	458	467	448	430	486	399
Y	31	31	34	33	31	29
Zr	203	222	275	261	184	213
Nb	11	13	22	16	10	10
Cs	1.5	1.5	1.4	1.3	0.7	1.0
Ba	479	537	584	586	373	480
La	26.4	29.4	32.7	32.5	23.3	28.0
Ce	58.2	64.9	71.0	70.7	53.7	63.2
Pr	7.48	8.23	8.95	8.55	7.01	7.61
Nd	31.90	34.14	36.25	35.35	29.86	31.1
Sm	7.21	7.57	7.76	7.35	6.71	6.49
Eu	2.16	2.29	2.31	2.35	2.10	1.79
Gd	8.26	8.61	8.89	9.00	7.80	7.37
Tb	1.09	1.10	1.21	1.05	1.02	0.88
Dy	5.80	5.87	6.03	6.11	5.84	5.24
Ho	1.14	1.17	1.20	1.16	1.11	0.94
Er	3.45	3.50	3.61	3.52	3.46	3.12
Tm	0.44	0.44	0.47	0.43	0.43	0.38
Yb	3.03	3.14	3.34	3.38	2.92	2.97
Lu	0.47	0.47	0.50	0.43	0.45	0.35
Hf	5.2	6.0	6.9	6.5	4.4	6.9
Pb	8.7	9.3	10.3	10.0	5.4	8.8
Th	4.8	5.7	8.1	6.1	3.7	4.6
U	1.1	1.2	1.3	1.5	0.9	1.3

Table 4. Major and trace-element (in ppm) compositions of Ho dark glassy material and pumice

Lake	LC	LM	LTr	LEl	LM	LM	LM
Section	AT6	AT7	AT12	BT7	AT7	AT7	AT7
Depth (cm)	67-74	0-15	0-40	10-17	0-15	0-15	0-15
n	5	1	1	1	6	9	2
Phase	Black Glass	Black Glass	Black Glass	Black Glass	Mafic Pumice	Intermediate Pumice	Felsic Pumice
SiO_2	54.95	-	-	-	57.66	59.30	65.75
TiO_2	2.03	-	-	-	1.73	1.60	0.90
Al_2O_3	15.70	-	-	-	15.89	15.91	15.48
FeO	9.09	-	-	-	7.99	7.10	4.35
MnO	0.18	-	-	-	0.16	0.17	0.14
MgO	3.52	-	-	-	2.99	2.52	1.08
CaO	6.90	-	-	-	5.87	5.24	2.56
Na_2O	5.30	-	-	-	5.21	5.54	6.64
K_2O	1.54	-	-	-	1.83	2.04	2.90
P_2O_5	0.80	-	-	-	0.67	0.59	0.21
Total	100	-	-	-	100	100	100
Ti	11527	8995	8257	11121	10311	8620	5940
V	340	252	215	328	254	195	104
Cr	61	24	15	32	15	12	13
Mn	1343	1173	1091	1366	1284	1181	1017
Co	27	14	15	26	56	75	30
Ni	46	17	21	34	16	17	16
Cu	204	31	34	38	42	39	30
Zn	133	133	106	120	121	114	111
Rb	34	43	44	22	45	51	64
Sr	525	440	392	487	459	399	290
Y	32	33	33	31	36	36	38
Zr	182	263	228	175	260	287	362
Nb	9	13	12	8	13	15	18
Cs	0.6	-	1.2	-	1.1	1.3	1.7
Ba	456	502	487	306	559	604	720
La	39.0	34.7	31.7	24.3	34.5	34.9	40.7
Ce	80.7	79.2	70.1	56.3	76.8	78.1	90.1
Pr	10.08	9.18	8.62	7.13	9.73	10.04	10.74
Nd	42.46	33.9	34.7	30.7	40.84	41.58	43.45
Sm	9.21	7.32	7.62	6.58	8.84	9.14	9.50
Eu	2.68	2.13	2.06	2.03	2.55	2.58	2.50
Gd	10.24	7.94	8.41	7.27	10.11	10.40	11.07

Tb	1.21	1.03	1.06	1.01	1.28	1.31	1.35
Dy	6.42	5.41	5.55	5.26	7.07	7.03	7.18
Ho	1.24	1.01	1.11	1.00	1.31	1.39	1.48
Er	3.81	3.13	3.33	3.13	4.17	4.41	4.38
Tm	0.41	0.27	0.41	0.32	0.50	0.52	0.60
Yb	2.92	2.79	2.75	2.65	3.50	3.80	4.05
Lu	0.46	0.40	0.45	0.37	0.54	0.56	0.64
Hf	4.7	5.5	5.3	3.9	6.2	7.2	8.6
Pb	12.1	8.1	10.0	5.3	9.3	10.5	13.4
Th	5.4	4.8	5.8	3.3	5.5	6.0	7.3
U	1.4	1.0	1.2	0.6	1.3	1.4	1.8
87Sr/86Sr	0.704472	-	-	-	-	-	0.704453

Table 5. Weight percent SiO_2, strontium concentrations and strontium isotopic compositions for the Ho, H1, H2, and 1991 Hudson eruptions

Eruptive Event	Ho	Ho	1991 AD	H2	H2	H1	H1	H1	H1	H1
Material	Pumice	Glass	Ash	Pumice	Ash	Pumice	Ash	Tephra	Tephra	Tephra
SiO_2 (wt %)	65.75	54.95	51.12	64.3	65.12	61.12	61.88	61.88	61.76	60.61
Sr (ppm)	290	525	510	227	243	382	369	361	374	392
$^{87}Sr/^{86}Sr$	0.704453	0.704472	0.70437	0.70444	0.70445	0.7045	0.70451	0.70452	0.70451	0.70448

Table 6. Representative electron microprobe analysis of pyroxene and olivine phenocryst from the Ho eruption

Lake	Section	Depth (cm)	Phase	SiO_2	TiO_2	Al_2O_3	Fe_2O_3	MnO	MgO	CaO	Na_2O	Total	En	Wo	Fs	Fo	Fa
LM	AT7	0-15	ol	37.91	0.07	0.04	23.94	0.39	36.05	0.35	0.00	98.8	-	-	-	72.9	27.1
LC	AT6	67-74	ol	37.73	0.06	0.02	25.50	0.43	34.92	0.26	0.00	98.9	-	-	-	70.9	29.1
LC	AT6	67-74	ol	37.81	0.04	0.00	24.83	0.46	35.85	0.18	0.02	99.2	-	-	-	72.0	28.0
LC	AT6	67-74	ol	38.74	0.06	0.01	22.42	0.45	37.76	0.27	0.00	99.7	-	-	-	75.0	25.0
LC	AT6	67-74	ol	37.71	0.04	0.03	25.07	0.45	36.68	0.23	0.02	100.2	-	-	-	72.3	27.7
LEl	BT7	10--17	ol	36.67	0.11	0.34	26.35	0.47	33.86	0.48	0.03	98.3	-	-	-	69.6	30.4
LEl	BT7	10--17	ol	36.25	0.07	0.10	28.64	0.57	32.12	0.28	0.00	98.0	-	-	-	66.7	33.3
LM	AT7	0-15	cpx	49.93	1.60	4.08	13.48	0.35	15.98	12.36	0.31	98.1	49.3	27.4	23.3	-	-
LM	AT7	0-15	cpx	49.15	1.43	3.90	11.36	0.39	15.43	16.56	0.42	98.7	45.8	35.3	18.9	-	-
LC	AT6	67-74	cpx	48.27	1.62	4.16	10.14	0.24	14.40	19.38	0.36	98.6	42.3	40.9	16.7	-	-
LC	AT6	67-74	cpx	48.06	1.84	4.54	11.65	0.39	15.27	16.30	0.38	98.4	45.6	35.0	19.5	-	-
LC	AT6	67-74	cpx	47.06	2.01	4.90	9.60	0.27	13.42	19.79	0.36	97.4	40.6	43.1	16.3	-	-
LC	AT6	67-74	cpx	51.41	0.72	1.63	10.26	0.29	16.29	16.63	0.21	97.5	47.9	35.2	16.9	-	-
LEl	BT7	10--17	cpx	47.73	2.01	4.58	10.92	0.30	13.44	18.09	0.48	97.5	41.3	39.9	18.8	-	-
LEl	BT7	10--17	cpx	49.20	1.71	3.68	11.72	0.37	15.67	15.83	0.34	98.5	46.6	33.8	19.6	-	-
LM	AT7	0-15	opx	51.65	0.19	0.47	23.23	1.32	20.29	1.66	0.01	98.8	58.8	3.5	37.8	-	-
LM	AT7	0-15	opx	51.65	0.17	0.38	23.07	1.31	21.01	1.71	0.04	99.3	59.7	3.5	36.8	-	-
LM	AT7	0-15	opx	53.23	0.30	0.56	22.17	1.22	21.41	1.64	0.04	100.6	61.1	3.4	35.5	-	-

Table 7. Representative electron mircoprobe analyses of plagioclase phenocrysts from the Ho eruption

Lake	Section	Depth (cm)	Mineral type	SiO_2	Al_2O_3	FeO	CaO	Na_2O	K_2O	MgO	MnO	Total	An	Ab	Or
LM	AT7	0-15	Grains	54.30	29.69	0.82	11.13	4.88	0.21	0.10	0.00	101.1	55.1	43.7	1.3
LM	AT7	0-15	Grains	54.76	28.74	0.96	10.73	4.89	0.30	0.16	0.00	100.5	53.8	44.4	1.8
LM	AT7	0-15	Grains	58.09	26.03	1.09	8.00	6.16	0.49	0.11	0.02	100.0	40.5	56.5	2.9
LC	AT6	67-74	Microlites	53.02	29.73	0.88	11.33	4.56	0.18	0.11	0.00	99.8	57.2	41.7	1.1
LC	AT6	67-74	Microlites	55.70	28.83	0.91	10.23	5.29	0.23	0.11	0.03	101.3	50.9	47.7	1.3
LC	AT6	67-74	Microlites	52.68	29.47	0.96	11.59	4.57	0.17	0.15	0.00	99.6	57.8	41.3	1.0
LC	AT6	67-74	Microlites	54.65	28.79	0.88	10.57	5.17	0.21	0.11	0.00	100.4	52.4	46.3	1.3
LC	AT6	67-74	Microlites	54.25	29.65	0.75	11.03	4.95	0.21	0.11	0.00	101.0	54.5	44.2	1.2
LC	AT6	67-74	Microlites	53.51	29.34	0.59	10.97	4.96	0.18	0.08	0.00	99.6	54.4	44.5	1.0
LEl	BT7	10-17	Microlites	59.41	21.86	0.38	6.88	6.09	0.43	0.04	0.00	95.1	37.4	59.8	2.8
LEl	BT7	10-17	Microlites	58.79	26.00	0.35	6.97	7.03	0.42	0.03	0.02	99.6	34.5	63.0	2.5
LEl	BT7	10-17	Microlites	56.31	27.97	0.86	9.53	5.49	0.30	0.09	0.01	100.6	48.1	50.1	1.8

APPENDIX B: Tables

Table 1A. Trace-element compositions (in ppm) of the Valmont Dike, Boulder Colorado

Sample	VMD 8-14-14	VMD 7-9-14	vmd 17 5-8-14	VMD 16	VMD 15	VMD 14
Ti	6639	6500	6303	6096	6414	6451
V	382	398	317	366	356	309
Cr	78	85	82	75	82	76
Mn	1632	1772	1501	1615	1646	1666
Co	42	43	35	39	38	36
Ni	39	57	52	59	68	34
Cu	202	212	179	197	198	187
Zn	168	145	123	135	143	142
Rb	98	108	97	99	107	89
Sr	984	1081	959	965	1131	1053
Y	27	29	24	25	30	26
Zr	147	154	145	140	156	151
Nb	20	21	20	30	21	19
Cs	2.9	3.1	2.8	3.4	3.2	2.5
Ba	855	934	889	860	925	910
La	39.7	42.9	40.6	38.5	41.7	40.8
Ce	80.3	87.0	83.3	76.5	87.3	84.2
Pr	9.69	10.66	10.04	9.74	10.97	10.29
Nd	38.69	42.43	38.15	38.75	42.79	42.98
Sm	8.17	8.77	7.84	7.89	8.79	8.03
Eu	2.62	2.62	2.08	2.44	2.52	2.25
Gd	11.48	9.54	8.84	8.39	9.99	8.20
Tb	1.12	1.07	0.91	1.04	1.07	0.90
Dy	5.09	5.57	4.76	5.17	5.55	4.99
Ho	0.96	1.07	1.00	1.04	0.98	0.92
Er	3.11	3.27	3.03	2.98	3.44	2.97
Tm	0.40	0.42	0.34	0.45	0.34	0.37
Yb	2.62	2.79	2.64	2.65	2.94	2.56
Lu	0.40	0.30	0.33	0.44	0.37	0.37
Hf	4.0	4.0	3.9	5.6	4.0	3.7
Ta	3.8	5.5	1.6	16.7	4.0	7.2
Pb	14.0	15.6	18.1	15.1	16.0	16.2
Th	8.3	8.3	8.8	10.1	8.3	9.2
U	2	3	2	3	3	3

Table 1A. Trace-element compositions (in ppm) of the Valmont Dike, Boulder Colorado

Sample	VMD 13	VMD 12	VMD 11	VMD 10	VMD 9	VMD 8
Ti	5806	6490	7099	5883	6200	5943
V	302	311	335	308	308	345
Cr	75	78	89	73	74	78
Mn	1591	1578	1729	1596	1634	1559
Co	35	35	38	36	36	38
Ni	50	34	31	44	45	53
Cu	189	190	199	183	195	169
Zn	127	131	122	124	130	134
Rb	95	96	101	89	91	87
Sr	955	936	1061	945	967	919
Y	26	26	27	23	25	24
Zr	129	139	148	129	134	127
Nb	20	18	20	17	17	18
Cs	2.9	2.6	2.8	2.7	2.7	2.6
Ba	802	792	887	821	841	800
La	38.3	38.0	40.3	35.6	35.9	35.7
Ce	78.4	76.6	81.1	72.5	73.1	72.1
Pr	9.57	9.30	9.93	8.97	9.01	8.81
Nd	39.18	36.77	39.70	37.76	37.31	35.74
Sm	8.16	7.59	8.14	8.05	7.11	8.29
Eu	2.59	2.15	2.11	2.10	2.09	2.59
Gd	9.16	8.25	8.05	8.48	7.99	9.01
Tb	1.02	0.84	0.89	0.93	0.83	0.92
Dy	5.03	4.61	4.99	4.63	4.90	4.79
Ho	0.92	0.87	0.88	0.89	0.81	0.87
Er	3.07	2.80	2.85	2.85	2.59	2.77
Tm	0.37	0.32	0.37	0.32	0.27	0.26
Yb	2.62	2.38	2.52	2.37	2.75	2.23
Lu	0.37	0.31	0.36	0.33	0.31	0.32
Hf	4.1	3.4	4.0	3.4	3.5	3.6
Ta	5.1	6.1	5.6	4.1	3.4	5.5
Pb	14.2	13.0	15.2	16.1	14.2	12.9
Th	10.6	7.7	8.1	7.7	7.6	8.1
U	2	2	3	2	2	3

Table 1A. Trace-element compositions (in ppm) of the Valmont Dike, Boulder Colorado

Sample	VMD 7	VMD6	VMD 5	VMD4	VMD 3	VMD 2
Ti	6104	5619	5961	5900	5711	5846
V	312	398	289	273	253	291
Cr	69	73	81	69	72	70
Mn	1486	1644	1698	1595	1561	1549
Co	36	40	40	39	35	38
Ni	49	45	66	61	56	62
Cu	168	178	191	186	174	185
Zn	122	140	134	113	72	118
Rb	90	88	99	96	88	104
Sr	906	922	1032	1003	942	1031
Y	26	23	25	25	22	25
Zr	135	118	141	140	132	141
Nb	19	18	20	19	19	20
Cs	2.8	2.5	3.1	2.7	2.9	2.9
Ba	775	818	910	877	843	883
La	38.0	35.6	35.6	38.1	35.0	39.3
Ce	78.4	76.5	74.9	75.8	74.3	78.6
Pr	9.58	9.13	8.90	9.34	8.71	9.08
Nd	38.23	34.33	37.80	39.70	36.93	36.82
Sm	7.98	8.02	7.62	7.47	7.07	7.26
Eu	2.55	2.41	2.10	2.08	1.76	2.03
Gd	8.71	8.81	8.06	7.32	6.96	7.60
Tb	0.99	0.88	0.93	0.91	0.79	0.87
Dy	4.88	4.87	4.88	5.21	4.35	4.63
Ho	0.95	0.92	0.91	0.98	0.84	0.88
Er	2.93	2.90	2.79	2.85	2.48	2.62
Tm	0.37	0.40	0.36	0.32	0.30	0.34
Yb	2.55	2.51	2.44	2.45	2.36	2.24
Lu	0.39	0.36	0.32	0.33	0.28	0.32
Hf	3.6	3.4	4.5	3.6	3.6	3.3
Ta	1.7	1.1	2.4	1.1	0.9	1.0
Pb	13.4	14.4	11.7	15.2	14.3	15.6
Th	8.0	7.5	8.0	8.2	7.3	7.6
U	2	2	2	2	2	4

Table 1A. Trace-element compositions (in ppm) of the Valmont Dike, Boulder Colorado

Sample	VMD 1	STDEV	Average	vmd control
Ti	6131	370	6163	6610
V	284	41	323	387
Cr	78	5	77	84
Mn	1640	72	1615	1640
Co	40	2	38	45
Ni	75	12	52	56
Cu	196	12	188	216
Zn	180	22	132	205
Rb	101	6	96	105
Sr	1002	62	989	1042
Y	25	2	25	28
Zr	141	10	139	157
Nb	19	3	20	36
Cs	2.9	0.2	2.8	3.1
Ba	855	47	857	900
La	36.1	2.4	38.2	42.4
Ce	76.2	4.6	78.3	87.7
Pr	8.79	0.65	9.50	10.37
Nd	38.34	2.28	38.55	40.07
Sm	7.09	0.51	7.86	10.14
Eu	2.04	0.26	2.27	3.34
Gd	7.41	1.05	8.54	14.28
Tb	0.82	0.09	0.93	1.26
Dy	4.45	0.32	4.91	5.94
Ho	0.80	0.07	0.92	1.03
Er	2.56	0.24	2.89	3.49
Tm	0.28	0.05	0.35	0.39
Yb	2.21	0.20	2.52	2.70
Lu	0.30	0.04	0.34	0.39
Hf	3.5	0.5	3.8	6.8
Ta	1.4	3.7	4.1	20.1
Pb	15.2	1.4	14.8	15.4
Th	7.0	0.9	8.2	12.6
U	2	0.5	2	2

APPENDIX C: Figures

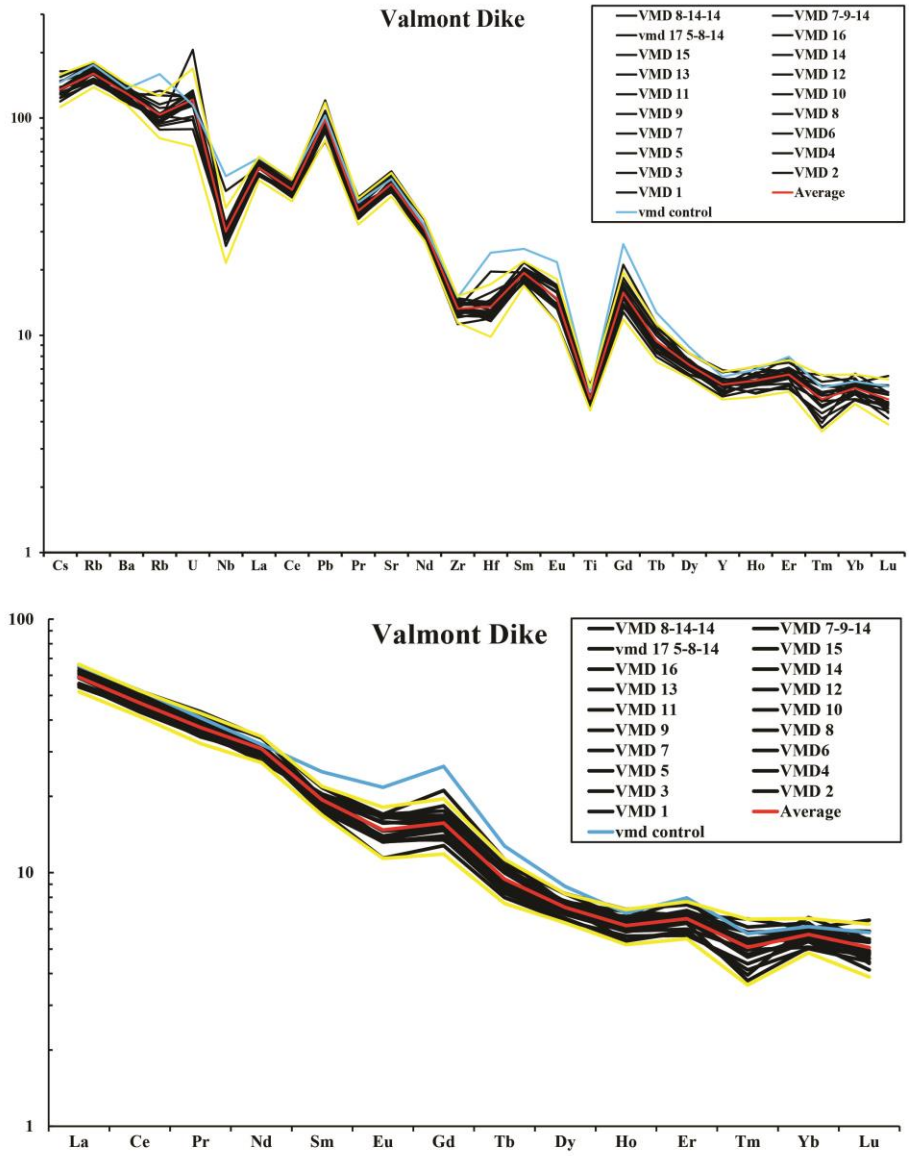

Figure 1A a) Primitive mantle-normalized trace-element diagram and b) primitive mantle-normalized REE plot for 19 analyses of Valmont Dike, Boulder Colorado (Normalization factors are taken from McDonough and Sun (1995)). The average of the 19 analyses (red), ±2-sigma of the mean (yellow), and an independent analysis of the Valmont Dike, obtained from ACT Labs (blue). Normalization factors P through Zr in ppm and Nb to U in ppb. P=90; K=240; Ti=1,205: Rb=0.600; Sr=19.9; Y=4.30; Zr=10.5; Nb=658; Cs=21; Ba=6,600; La=648; Ce=1,675; Pr=254; Nd=1,250; Sm=406 ; Eu=154; Gd=544; Tb=99; Dy=674; Ho=149 ; Er=438; Tm=68; Yb=441; Lu=67.5; Hf=283; Th=79.5; U=20.